DETERMINATION OF APPLIED STRESSES IN RAILS USING THE ACOUSTOELASTIC EFFECT OF ULTRASONIC WAVES

A Thesis

by

SHAILESH GOKHALE

Submitted to the Office of Graduate Studies of
Texas A&M University
in partial fulfillment of the requirements for the degree of

MASTER OF SCIENCE

December 2007

Major Subject: Civil Engineering

DETERMINATION OF APPLIED STRESSES IN RAILS USING THE ACOUSTOELASTIC EFFECT OF ULTRASONIC WAVES

A Thesis

by

SHAILESH GOKHALE

Submitted to the Office of Graduate Studies of
Texas A&M University
in partial fulfillment of the requirements for the degree of

MASTER OF SCIENCE

Approved by,

Chair of Committee,	Stefan Hurlebaus
Committee Members,	Gary Fry
	Don Bray
Head of Department,	David Rosowsky

December 2007

Major Subject: Civil Engineering

ABSTRACT

Determination of Applied Stresses in Rails Using the Acoustoelastic Effect

of Ultrasonic Waves. (December 2007)

Shailesh Gokhale, B.E., Mumbai University, Mumbai, India

Chair of Advisory Committee: Dr.- Ing. Stefan Hurlebaus

This research develops a procedure to determine the applied stresses in rails using the acoustoelastic effect of ultrasonic waves. Acoustoelasticity is defined as the stress dependency of ultrasonic wave speed or wave polarization. Analytical models are developed that predict the acoustoelastic effect for longitudinal waves, shear waves, Lamb waves, and Rayleigh waves. Using a programming tool, a numerical simulation of the models is generated to obtain the stress dependent curves of wave velocity and polarization of the various ultrasonic waves propagating in rail steel. A comparison of the sensitivity of the acoustoelastic effect is made to determine the feasibility of ultrasonic waves for further study. Rayleigh waves are found to be most sensitive to stress change. Rayleigh waves are generated using ultrasonic transducer and detected using a laser Doppler vibrometer (LDV). The LDV measures the in-plane and out-of-plane velocities. Polarization is defined as the ratio of in-plane and out-of-plane displacements. Initially, polarization is determined for the specimen in unstressed condition. Thereafter, the rail specimen is stressed in a compression testing machine, the experiment repeated, and the polarization determined. Thus, Rayleigh wave polarization is obtained as a function of applied stress. Finally, the change in polarization obtained experimentally is compared with the analytical model.

DEDICATION

To my parents Veena and Ashok Gokhale who always supported me and encouraged me throughout my graduate studies at Texas A&M University.

ACKNOWLEDGEMENTS

I would like to express my heartiest gratitude to Dr. Stefan Hurlebaus for his support, guidance and patience throughout this research. I also sincerely acknowledge the contribution of Dr. Gary Fry and Dr. Don Bray for their interest in my research and valuable guidance in preparing this document.

I wish to thank the Dwight David Eisenhower Transportation Fellowship Program for their support. I also thank the Civil Engineering Department for providing financial support during my graduate studies at Texas A&M University. A special thanks to Dr. Keating for providing testing equipment at the High Bay Lab. I also acknowledge the help offered by Vikrant Palan from Polytec, who provided the laser Doppler vibrometer free of charge.

A special thanks to my dear Sucheta, sister Shilpa and all friends for their prayers and encouragement to complete this research.

TABLE OF CONTENTS

CHAPTER Page

CHAPTER Page

LIST OF FIGURES

FIGURE Page

FIGURE Page

FIGURE Page

LIST OF TABLES

TABLE Page

CHAPTER I

INTRODUCTION

1.1. Background

Continuous welded rails (CWR) have become more popular than jointed tracks because of their high strength which facilitates smoother rides and higher speeds. Although the laying of welded rails might be a little expensive, they prove to be more economical in the long-term due to their low maintenance costs.

CWR are typically long members which are susceptible to failure caused by temperature changes. Rails are subjected to compressive stresses as they expand in hot weather and tensile stresses as they contract in cold weather. Such rail temperature changes can lead to buckling or fracture of rails and eventually cause derailment of high speed trains. It is observed that a rise in rail temperature of 10°C generates a compressive load of 18 tons (Tunna, 2000). Fig. 1.1 shows an example of buckling due to thermal stresses.

Fig. 1.1. Buckling of tracks due to thermal stresses *(Railway Investigation Report, Transportation Safety Board of Canada (TSB), 2002 and 2003)*

This thesis follows the style of the *ASCE Journal of Structural Engineering.*

To avoid this problem, engineers install the rails at a temperature somewhere in between the extreme hot and cold temperatures of that region. This temperature is referred to as the stress free temperature (SFT). If the temperature is lower than SFT, tension builds in the rail and can cause fracture in the rail. On the other hand if the temperature is above SFT, compression is observed in the rail and can cause the rails to buckle. It is therefore crucial to know the SFT at which the longitudinal force in the rail will be zero.

Stress free temperature or rail neutral temperature is defined as the temperature at which the longitudinal force in the rail is zero. The force in a rail of cross section *A*, elastic modulus *E*, thermal coefficient α, and subjected to a temperature change of ΔT is given by

$$P = AE\alpha\Delta T, \tag{1.1}$$

where the temperature change ΔT corresponds to the change in temperature from the neutral temperature. An example by Kish and Samavedam (2005) presents the importance of maintaining stress free temperature. Consider a CWR segment with a stress free temperature of $T_n = 25^{\circ}\mathrm{C}$. If the track buckling forces are generated due to a temperature change of $\Delta T = 15^{\circ}\mathrm{C}$, then buckling occurs when the rail temperature reaches $40^{\circ}\mathrm{C}$. Due to some reason, if the stress free temperature drops to $15^{\circ}\mathrm{C}$, the rail would buckle at a lower temperature of $30^{\circ}\mathrm{C}$. SFT may change due to several reasons as explained in a later part of this section.

The stress free temperature is actually related to the stress in the rail since it is merely the ambient temperature where a fixed length of rail has no compressive or tensile stresses. In other words even if the ambient temperature is different, SFT can be induced in the rail by manipulating the stress in the rails while laying or repairing the

tracks. The direct relation between rail neutral temperature and longitudinal force in the rail is given by

$$T_n = T_a - \frac{\sigma}{E\alpha}, \tag{1.2}$$

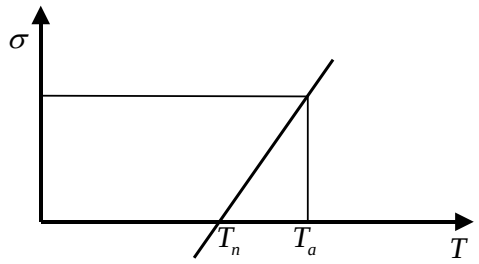

Fig. 1.2. Rail neutral temperature

where T_n is the rail neutral temperature, T_a is the ambient temperature, and σ is the stress. Fig. 1.2 shows this relationship. Thus, if the longitudinal stress in the rail is determined and the ambient temperature known, SFT can be determined using Eq. (1.2).

Following are the factors affecting the stress free temperature:

- *Rail Longitudinal Movement*

  The continuous running of trains, braking and accelerating actions along with temperature gradients along the rail can cause the stress free temperature to change.

- *Track Lateral Shift*

  The lateral shift, sometimes referred to as “rail breathing”, occurs due to repeated lateral loads under running conditions and thermal loads on curves.

- *Track Vertical Settlement*

  Repeated vertical wheel loads and high impacts on poorly supported tracks can cause vertical settlements which eventually affect the stress free temperature.

- *Maintenance Operations*

  Maintenance operations such as lining, lifting, tamping, repairing defective or broken rails, also affect the longitudinal force state in the rail and alter the stress free temperature.

1.2. Scope and Objective

The objective of this research is to investigate a potential technique to determine the applied stresses in rails using the acoustoelastic effect of ultrasonic waves under controlled laboratory conditions. The proposed methodology utilizes the well-known acoustoelastic effect of ultrasonic waves to determine the longitudinal stress in the specimen.

Analytical models examining the acoustoelastic effect of different ultrasonic waves are developed. The ultrasonic waves studied are longitudinal waves, shear waves, Lamb waves, and Rayleigh waves. Analytical study with these different ultrasonic waves aided in deciding the feasibility of using a specific ultrasonic wave from the point of view of sensitivity of the acoustoelastic effect. The experimental procedure uses a transducer for generation, and laser Doppler vibrometer (LDV) system for detection of Rayleigh waves. The specimen is stressed under fixed supports to study the changes in polarization of the Rayleigh wave and wave velocity with stress. The experimental results are compared with the results from the model.

The successful realization of this stress determination technique can be further developed to a nondestructive, noncontact stress free temperature measuring technique.

1.3. Organization of Thesis

This thesis is divided into seven chapters. Chapter I gives an introduction to the topic and presents a general idea on the problem under study. Chapter II describes a review of earlier research on the acoustoelastic effect of ultrasonic waves and various techniques for stress measurement. Chapter III briefly discusses the theory on elasticity and wave propagation in solids. In Chapter IV, analytical models describing the acoustoelastic effect of ultrasonic waves are derived. Chapter V describes the routine to setup numerical simulation for determining the theoretical values of the acoustoelastic effect. Also discussed are the important results of the simulation. Chapter VI describes the experimental procedure for measuring the acoustoelastic effect and thereby determining the applied stress. This chapter summarizes the experimental setup, discusses the principles involved in measuring the acoustoelastic effect and presents the experimental results and conclusion. The final chapter summarizes the work, discusses important conclusions, and presents recommendations for future work.

CHAPTER II

LITERATURE REVIEW

This chapter provides a background on topics pertaining to stress free temperature, acoustoelastic effect, and stress measurement in solids. The chapter includes general information and a review of previous research on these topics.

2.1. Acoustoelasticity

The fundamental principle functional in this research is the acoustoelastic effect of ultrasonic waves. Acoustoelasticity has been the subject under study for more than half a century. Acoustoelastic effect or acoustoelasticity is the dependency of ultrasonic wave speed and polarization on stress. Ultrasonics has long been a successful resource for studying the relationship between stress and the characteristics of wave propagation. Cauchy's theory of small deformations is restricted to elastically deformed medium. Acoustoelasticity is based on a continuum theory of small disturbances superimposed on an elastic material as formulated by Cauchy. It is a well known fact that, the elastic theory of small deformation becomes invalid if the material under stress is plastic or if the deformations are large enough to make the infinitesimal theory invalid.

A theory of finite deformations was introduced by Murnaghan (1951). This theory made two important revisions from the infinitesimal theory. Firstly, due to large deformations, the initial and final coordinates are not interchangeable. Secondly, the strain energy terms were revised in order to express the terms in the initial or in the final coordinates independently. Murnaghan (1951) introduced three third order elastic (TOE) constants, l, m , and n for an isotropic body in addition to the second order coefficients also known as second-order Lamé constants, λ , and μ . The application of Murnaghan's finite theory to the propagation behavior of acoustic waves in an elastically deformed material was completed by Toupin and Bernstein (1961). They also show how the

measured acoustoelastic effect can be used to determine the TOE constants for an isotropic material. The theory of acoustoelasticity was extended to orthotropic media by Pao and Gamer (1985). Hughes and Kelly (1953) derived expressions for the speeds of elastic waves in a stressed solid using Murnaghan's theory. The effect of compressive stresses and hydrostatic pressure on polystyrene, Pyrex glass, and iron was investigated and velocities of longitudinal and shear waves determined as a function of stress. Hayes and Rivlin (1961) were the first to provide the theory on acoustoelasticity of surface waves, namely, Rayleigh waves and Love waves. In this work, the theory of finite deformations is applied to study the propagation of surface waves in a semi-infinite body subjected to a static, pure homogenous deformation.

Crecraft (1966) summarizes different methods of measuring stress-induced velocity changes. Hughes and Kelly (1953) measured the velocity changes for polystyrene, Pyrex glass, and Armco iron and determined the acoustoelastic constants using the pulse-echo technique. This method simply measured the time taken by a pulse to travel through the specimen as seen on the oscilloscope. This technique obviously lacked precision and a modification of this method by Bergman and Shahbender (1958) enabled a better sensitivity. The modified method transmitted a reference pulse through an ultrasonic delay line set to give the same delay as the specimen in the unstressed state. Another technique called the pulse superposition method uses the principle of matching the pulse repetition frequency (PRF) to an integral multiple of the travel time of a single pulse. This allows the series of received pulses to arrive in phase. The transit time can be determined from the PRF, the echo number, and averaging from the number of readings.

Crecraft (1966) uses the sing-around technique for measuring the stress-induced velocity changes for steel, aluminum and copper, using shear and longitudinal waves. This technique involves generating a pulse using a transducer and receiving the pulse with another transducer. The receiving transducer converts the mechanical energy into electrical energy which retriggers the generating transducer. Thus a pulse "sings-around"

the system at repetition rate associated with the travel time. As the stress in the specimen changes, the PRF varies inversely as the transit time.

Hirao et al. (1981) investigated the acoustoelastic effect for Rayleigh surface waves propagating in a homogenous isotropic material. Analytical and experimental validation was carried out for (i) uniform stress, and (ii) non-uniform stress distribution. The experimental data was obtained for a mild steel sample using the sing-around technique. The results revealed that under a uniform stress, Rayleigh waves are non-dispersive and change in velocity with stress is linear. For a non-uniform stress distribution, Rayleigh waves are dispersive with the dispersion effect more prominent at lower frequencies. Fig. 2.1 shows the experimental results.

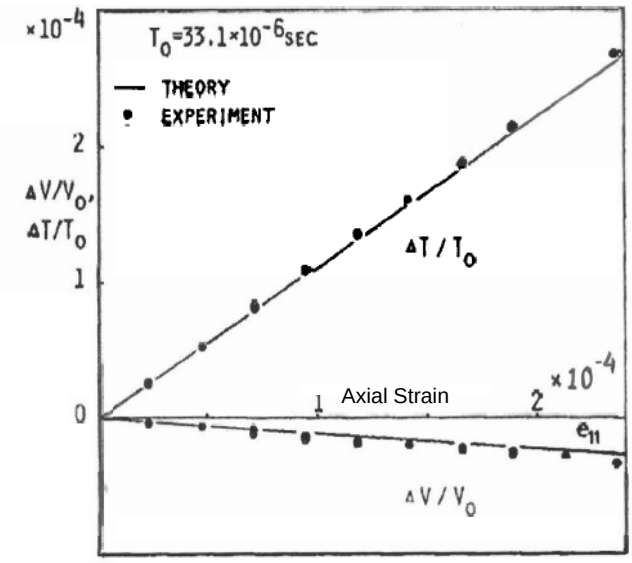

Fig. 2.1. Relative variation of Rayleigh wave transit time and velocity with uniaxial strain *(Hirao et al. (1981))*.

Egle and Bray (1976) measured the acoustoelastic and TOE constants for rail steel using longitudinal waves. The method employed contact transducers for the

generation and reception of longitudinal waves. Acoustoelastic constants for relative change in wave speed in five directions were determined. Sing-around technique, resonant frequency technique and pulse overlay technique were compared and it was found that the latter yielded most consistent results. Measured values of the acoustoelastic constants were found to be consistent with the predictions of Hughes and Kelly (1953).

Fukuoaka and Toda (1977) determined the acoustoelastic constants for aluminum, pure iron, and copper using shear transducers as transmitter and receiver and employing the sing-around technique. Their results demonstrate that, for aluminum and pure iron, ultrasonic velocity for transverse waves varies linearly to the applied stresses and for copper this relation is parabolic.

Another technique for wave excitation and detection is interferometry. This technique involves superimposing two waves resulting into an output wave that is different from the input waves in phase and amplitude. The output wave can be used to compare the differences between the two input waves. Earlier interferometry techniques used electrical signals from a train of pulse echoes produced by multiple reflections in the specimen and added to another train. The former train could be from a stressed specimen and the latter could be from an unstressed specimen. This technique was investigated by Espinola and Waterman (1958). The velocity differences lead to phase cancellation of some echoes and addition of others. Hurlebaus and Jacobs (2006) developed an effective dual probe laser interferometer that has the advantage of making two independent and simultaneous measurements with a reduced number of optical components. This technique was developed to measure guided waves in a plate, or Lamb waves.

The latest development in interferometry is laser Doppler vibrometry. It is based on the principle of measuring the Doppler shift of laser light scattering from a tiny spot on a vibrating body. The vibrating body reflects the laser beam and the velocity of

vibration is obtained by analyzing the Doppler shift using an optical interferometer. Junge et al. (2004) investigated the acoustoelasticity for aluminum using laser vibrometry. Rayleigh waves were generated using a transducer mounted on a plexiglass wedge and detected using a laser Doppler vibrometer. This technique enabled the simultaneous measurements of in-plane and out-of-plane velocities in an aluminum plate. The polarization of Rayleigh waves in unstressed and stressed specimen were determined and compared with the analytical values. The experimental results, however, did not conform to the analytical model. Fig. 2.2 shows the analytical results for the acoustoelastic effect of Rayleigh waves.

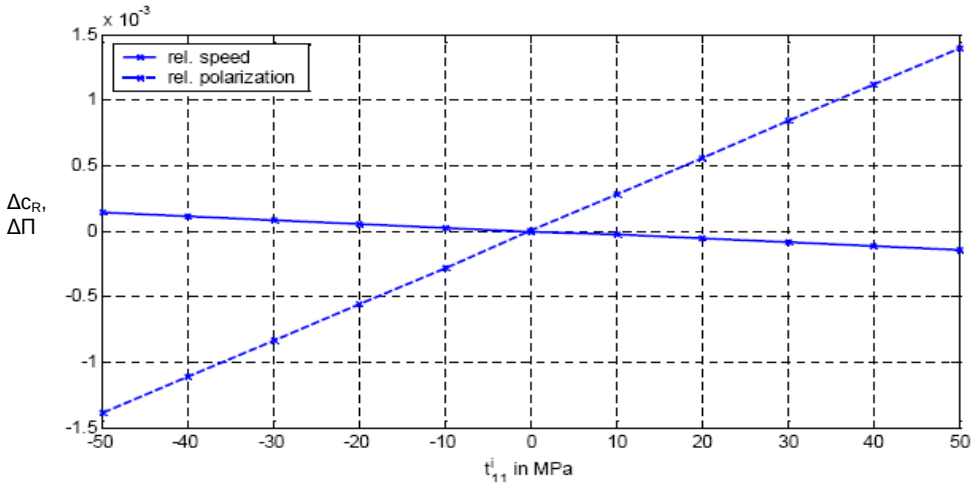

Fig. 2.2. Relative change of Rayleigh wave speed and polarization with uniaxial stress for aluminum (*Junge et al. (2004))*

It may be noted that all these techniques except laser interferometry, measure velocities using transit time of an ultrasonic wave. The disadvantage is that such techniques may be influenced by the material characteristics along the path of ultrasonic wave. Another shortcoming may be the irreproducibility of the contact conditions when the transducer is shifted from point to point on the specimen surface. Also, the contact transducers are not available under certain conditions such as high temperature. Hence, a

non-contact measuring technique would be most effective. This research uses a point-wise, reference free technique for measuring the stress induced velocity using laser Doppler vibrometry.

2.2. Stress Measurements Using Ultrasonics

In the past, various researchers have explored stress measurement techniques. Egle and Bray (1979) developed an ultrasonic probe for determination of the in-situ longitudinal stress measurement. The probe generates and receives longitudinal waves traveling along the longitudinal rail axis. A pulse overlay technique, similar to the pulse superposition technique is used to measure the travel time. Duquennoy et al. (1999) investigated residual stress measurement using Rayleigh waves. The stress profile along the thickness of aluminum sheets was investigated. The stress profiles were developed from the relative change in Rayleigh wave speed determined with a time of flight technique. The results were found similar when compared to a destructive method of stress determination. Bray and Leon (1985) describe a technique for measuring the longitudinal stresses in rail using head-waves. This technique measures bulk stresses and uses the time of flight technique to determine the velocity of bulk waves. Their paper makes an attempt at establishing the zero-force travel times so that the absolute stress in rails could be measured.

Husson et al. (1982) developed a method to determine surface stresses using Rayleigh waves. They used an edge-bonded transducer for excitation and electromagnetic transducers (EMAT) for detection using the pulse-superposition technique. Stress-acoustic coefficients for Rayleigh waves were determined by Lingfeng and Kobayashi (2000) using laser Doppler velocimetry. Jassby and Kishoni (1982) describe an experimental technique to measure the stress-acoustic coefficients of Rayleigh waves using the time of flight technique.

Over the years, different methods of identifying the stress free temperature in rails have been developed and practiced commercially. These techniques are time consuming, difficult, destructive, labor intensive and require contact with the rails. The traditional method is to cut the rail, measure the gap, calculate SFT, and re-weld the rail. A new technique that has been developed by Salient Systems, Inc. (Kish and Read, 2006) uses a strain gauge based remote sensing module fixed at the rail neutral axis and held in position by a bolt (Fig. 2.3). This device monitors and stores the rail temperature and stress at certain time intervals. This data is then transferred to a hand held, vehicle or train-mounted device and is uploaded to software where the data can be viewed and analyzed.

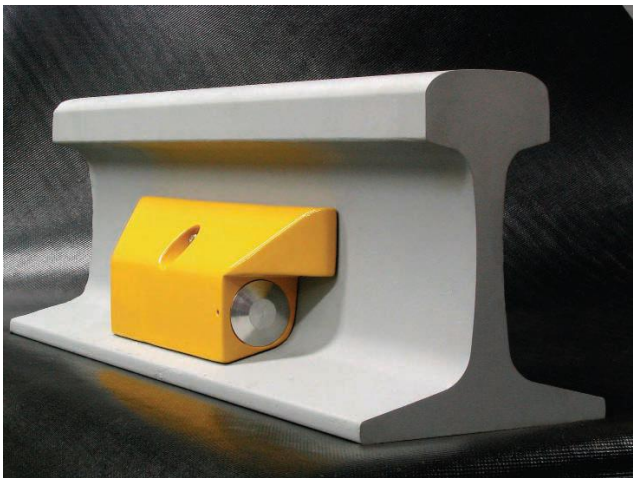

Fig. 2.3. Wireless Rail Stress Module *(www.salientsystems.com, 02/10/2007)*

Another method developed by Vortok International (Tunna, 2000) utilizes the rail's bending response as a measure of the longitudinal force in the rail. This method, although nondestructive, requires unclipping the rail, placing the Vertical Rail Stiffness Equipment (VERSE) in position, applying a set of loads on the rail, removing the equipment, reclipping the rail, and finally making the measurements. Eventually, this

method turns out to be time-consuming and labor intensive. Fig. 2.4 shows the VERSE system in place and ready for taking measurements.

Fig. 2.4. VERSE equipment (*www.vortok.co.uk, 02/01/2007)*

A recent development is the rail vibration based d'Stresen system (Kish and Read, 2006). This system uses the basic principle that the vibration amplitude of a bar clamped to the rail is proportional to the longitudinal force in the rail. The vibration amplitude is maximum when the stress in the rail is zero; therefore the SFT is determined. The validation studies demonstrate a good agreement between SFT determined using the strain gauge and using the vibration technique. However, the measurement concept is validated only with the rail in tension. While this system is based on a nondestructive excitation and measurement of vibrations in rails, the system is in contact.

Another technique investigated by Weaver and Damljanović (2004) makes use of the principle of sensitivity of bending rigidity to stress. This technique makes use of a laser scanning vibrometer to measure stress in rails. It measures the bending wave

number in rail in the stressed condition and compares it with the wavenumber of a rail without stress. Early experiments concluded that this technique requires very high precision equipment without which the experiments failed when carried out on the field at Transportation Technology Center, Inc. (TTCI).

The aim of this research is to investigate if laser vibrometry can be employed to measure the stress induced ultrasonic wave velocity changes and thereby determines the velocity as a function of applied stress. A lot of previous research has been carried out using either longitudinal or shear waves. This research also tries to explore the potential of Rayleigh waves and Lamb waves in stress determination. Successful completion of this research would allow the results to be used for developing a new technique for in situ SFT measurements.

2.3. Texture

Texture is defined as the preferred orientation of crystallites in a material. It is important to include the effect of variations in texture on stress measurement, since the texture of material has a profound effect on physical properties such as anisotropy and wave propagation. Texture types are classified as face centered cubic (FCC), body centered cubic (BCC), and hexagonal closed packed (HCP). Hot rolled steel has BCC crystal structure. When a material is subjected to deformation, there is a complex change of the crystal structure and gradual rearrangement, which results in a change in the anisotropy. As ultrasonic wave velocity is anisotropic, an observed anisotropy in the wave velocity could be inaccurately attributed to the presence of residual or applied stresses. Hence, it is recommended to establish an account of ultrasonic velocity as a function of the texture of the material. Allen and Sayers (1984) talk about an ultrasonic technique for including the effects of variable texture while determining residual stresses in steel. This technique uses the longitudinal wave in combination with two orthogonally polarized shear waves and evaluates the time delay of the three waves. MacDonald

(1980) presents a comparison of wave speeds for materials with different textures to demonstrate the effect of variable texture.

Texture can be measured by, either averaging over a large volume of polycrystalline aggregates or by measuring the orientation of individual crystals (Wenk and Houtte, 2004). Texture is determined using methods based on diffraction or using optical techniques. X-ray diffraction with a pole-figure geniometer, neutron diffraction, and electron diffraction are a few examples using the diffraction technique.

This research does not account for the variations in texture in the test sample. However, it is recommended to evaluate the effect of texture on wave velocity before applying any stress measurement technique on a large scale.

CHAPTER III

THEORY OF WAVE PROPAGATION

This chapter gives a brief review on the concept of wave propagation through solid media. Some basic relationships for a linear elastic continuum are discussed followed by a brief description of the various modes of propagation of ultrasonic waves in elastic media.

3.1. Different States of the Body

A solid body undergoes a series of deformations from a stress free state to a static deformation or a dynamic deformation. Based on such a deformation process Duquennoy et al. (1999) define three states of a body. The *natural* state of a body is a state of zero stress and zero strain. This is an ideal case and such state practically never exists. The body undergoes a static deformation due to residual stresses during the manufacturing processes or due to applied stresses. Such a state is referred to as the *initial* state of the body. Eventually, a dynamic deformation, for instance, an ultrasonic wave through the body gives rise to further stresses and this is referred to as the *present* or *final* state of a body. Fig. 3.1 shows the coordinate system followed in this thesis, where x_1 is the direction of propagation of the wave. Fig. 3.2 describes the relation between the three states of a body. The common Cartesian coordinate system as shown in Fig. 3.1 is used to refer the position of material points in the three states. The position vector $\boldsymbol{\xi}$ defines the position of a point in the natural state. Similarly $\boldsymbol{X}$ and $\boldsymbol{x}$ define the position in the *initial* and *final* states respectively.

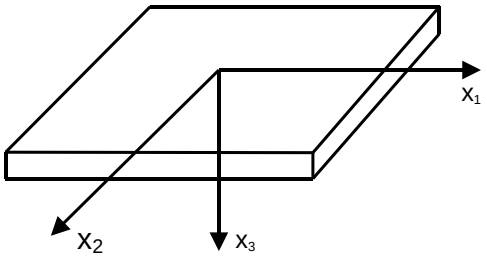

Fig. 3.1. Co-ordinate system

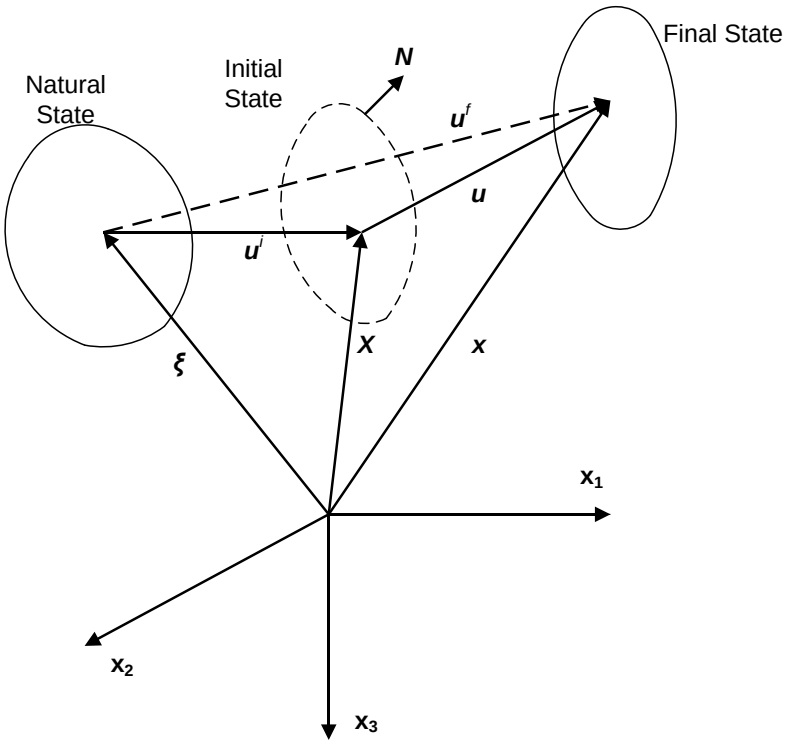

Fig. 3.2. Natural, initial and final states of a body (See FIG. 1 of Duquennoy et al. (1999))

The displacements of a point from one state to another can be described mathematically as

$$\begin{aligned} \boldsymbol{u}^i(\boldsymbol{\xi}) &= \boldsymbol{X} - \boldsymbol{\xi}\,, \\ \boldsymbol{u}^f(\boldsymbol{\xi},\boldsymbol{t}) &= \boldsymbol{x} - \boldsymbol{\xi}\,, \\ \boldsymbol{u}(\boldsymbol{\xi},\boldsymbol{t}) &= \boldsymbol{x} - \boldsymbol{X}\,. \end{aligned} \tag{3.1}$$

3.2. Background of Wave Propagation

3.2.1. Equations of Motion

The principle of balance of linear momentum states that the total force acting on the body equals the rate of change of momentum. This can be written mathematically as

$$\int_A t_m \mathrm{d}A + \int_V f_m \rho \mathrm{d}V = \frac{\mathrm{d}}{\mathrm{d}t}\int_V v_m \rho \mathrm{d}V\,, \tag{3.2}$$

where t_m represents the distribution of traction forces on the body, f_m are the internal body forces such as weight, ρ is the material mass density of a body of surface area A and volume V. Using Cauchy's stress equation

$$t_m = n_n T_{mn}\,, \tag{3.3}$$

and Gauss's divergence theorem

$$\int_A n_n u_n \mathrm{d}A = \int_V \frac{\partial u_n}{\partial x_n}\mathrm{d}V\,, \tag{3.4}$$

where n_n is an outward normal vector and T_{mn} is the stress tensor, the balance of linear momentum can be written as

$$\int_V \left(\frac{\partial T_{mn}}{\partial x_n} + \rho f_m - \rho \ddot{u}_m \right) \mathrm{d}V = 0\,, \tag{3.5}$$

where x_m denotes the direction in the coordinate system and u_m denotes the displacement in the x_m - direction. Assuming a continuous integrand, Eq. (3.5) will be satisfied if the integrand equals zero. Neglecting the body forces it follows from Eq. (3.5)

$$\frac{\partial T_{mn}}{\partial x_n} = \rho \frac{\partial^2 u_m}{\partial t^2}\,. \tag{3.6}$$

3.2.2. Stress-Strain Relationships

3.2.2.1. Hooke's Law

The generalized Hooke's law for an elastic material in three dimensional stress-state can be expressed as

$$T_{mn} = C_{mnpq} \frac{\partial u_p}{\partial x_q}, \tag{3.7}$$

where C_{mnpq} is the tensor of elastic constants. The 81 elastic constants drop down to 21 because of symmetric nature of the stress and strain tensors. In case of an isotropic material, the material properties are independent of direction. The elastic constants are then simply expressed as a combination of Lamé constants

$$C_{mnpq} = \lambda \delta_{mn} \delta_{pq} + \mu \left(\delta_{mp} \delta_{nq} + \delta_{mq} \delta_{np} \right), \tag{3.8}$$

where λ and μ are the second order elastic constants also known as Lamé constants, and δ_{ij} is Kronecker delta. Lamé constants are expressed in terms of Young's modulus *E*, and Poisson's ratio υ

$$\mu = \frac{E}{2(1+\upsilon)}, \qquad \text{and} \qquad \lambda = \frac{E\upsilon}{(1+\upsilon)(1-2\upsilon)}.$$

Substitution of Eq. (3.7) into Eq. (3.6) gives

$$C_{mnpq} \frac{\partial^2 u_p}{\partial x_n \partial x_q} = \rho \frac{\partial^2 u_m}{\partial t^2}. \tag{3.9}$$

Substitution of Eq. (3.8) into Eq. (3.9) leads to the following equations of motion

$$\mu \frac{\partial^2 u_m}{\partial x_n \partial x_n} + (\lambda + \mu) \frac{\partial^2 u_n}{\partial x_m \partial x_n} = \rho \frac{\partial^2 u_m}{\partial t^2}. \tag{3.10}$$

3.2.2.2. Elastic Constants

In the linear theory of elasticity, the propagation velocities of ultrasonic waves depend on the material properties such as mass density, stiffness coefficients and other parameters that are defined in the *natural* state. These parameters are assumed to remain

constant during any deformation. The velocities therefore depend only on the second order elastic constants. Thus, when the material is stressed, the second order constants cannot describe the change in the ultrasonic wave velocities due to such applied stress. In order to deal with changes in wave speeds due to stresses, a nonlinear behavior needs to be introduced. Such nonlinearity occurs due to large deformations and a nonlinear stress-strain behavior. The nonlinear theory takes into account the second order effect of strain and introduces the third-order elastic constants in addition to the second order Lamé constants. For an isotropic material like rail steel the elastic constant C_{mnpq} can be expressed in terms of the second-order elastic constants and the TOE constants as

$$\begin{aligned} C_{IJKL} &= \lambda\delta_{IJ}\delta_{KL} + \mu(\delta_{IK}\delta_{JL} + \delta_{IL}\delta_{JK}) \\ &+[(-\lambda+\upsilon_1)\delta_{IJ}\delta_{KL} + (-\mu+\upsilon_2)(\delta_{IK}\delta_{JL} + \delta_{IL}\delta_{JK})]\varepsilon_{MM} \\ &+2(\lambda+\upsilon_2)(\varepsilon_{IJ}\delta_{KL} + \varepsilon_{KL}\delta_{IJ}) \\ &+2(\mu+\upsilon_3)(\varepsilon_{IK}\delta_{JL} + \varepsilon_{IL}\delta_{JK} + \varepsilon_{JK}\delta_{IL} + \varepsilon_{JL}\delta_{IK}) \end{aligned}, \tag{3.11}$$

where $\upsilon_1,\ \upsilon_2,\ \upsilon_3$ are the TOE constants.

For an isotropic material the elastic constants matrix is given as (Jones, 1999)

$$C_{IJKL} = \begin{pmatrix} C_{11} & C_{12} & C_{12} & 0 & 0 & 0 \\ C_{12} & C_{11} & C_{12} & 0 & 0 & 0 \\ C_{12} & C_{12} & C_{11} & 0 & 0 & 0 \\ 0 & 0 & 0 & \frac{(C_{11}-C_{12})}{2} & 0 & 0 \\ 0 & 0 & 0 & 0 & \frac{(C_{11}-C_{12})}{2} & 0 \\ 0 & 0 & 0 & 0 & 0 & \frac{(C_{11}-C_{12})}{2} \end{pmatrix}, \tag{3.12}$$

where the constants C_{ij} can be obtained if Young's modulus E and Poisson's ratio υ for the material is known. Jones (1999) gives simple relations to derive these constants. For an isotropic material,

$$C_{11} = \frac{(1-\upsilon^2)}{E^2\Delta}, \quad C_{12} = \frac{\upsilon(1+\upsilon)}{E^2\Delta},$$

with

$$\Delta = \frac{(1-3\upsilon^2-2\upsilon^3)}{E^3}. \tag{3.13}$$

3.2.2.3. Index to Matrix Notation for Isotropic Case

Rose (2004) provides a simple rule to convert the elastic constants in the index form $\left(C_{mnpq}\right)$ to the matrix form $\left(C_{ij}\right)$. This rule is a useful tool while solving the Christoffel equation introduced in Chapter IV. The rule states that

- If $m = n$ then $i = m$; and if $p = q$ then $j = n$.
- If $m \neq n$ then $i = 9-(m+n)$ and if $p \neq q$ then $j = 9-(p+q)$.

For instance,

$C_{1111} = C_{11}$ where $m = n = p = q = 1$; using the above rule $i = j = 1$.

$C_{1311} = C_{51}$ where $m \neq n$ implies $i = 9-(m+n) = 5$ and $p = q = 1$ implies $j = 1$.

3.3. Ultrasonic Waves

Ultrasonics is the study and application of sound waves vibrating at frequencies greater than 20 kHz, i.e., beyond the range of human hearing. Ultrasonic waves serve numerous applications in the fields of medicine, defense and industries. The application that interests civil engineers is nondestructive testing, popularly known as 'NDT'. In solids, sound can propagate as longitudinal waves, shear waves, surface waves or guided waves. This section briefly discusses the nature of these waves.

3.3.1. Longitudinal Waves and Shear Waves

Longitudinal and shear waves are the two modes of propagation most widely used in ultrasonic testing. These waves travel in an unbounded solid. Fig. 3.3 (a) and (b) describe the propagation of longitudinal and shear waves, respectively. The displacement field for a longitudinal wave can be described by (Bedford and Drumheller, 1996)

$$\begin{aligned} u_1 &= u_1(x,t), \\ u_2 &= 0, \\ u_3 &= 0, \end{aligned} \tag{3.14}$$

and for shear waves

$$\begin{aligned} u_1 &= 0, \\ u_2 &= 0, \\ u_3 &= u_3(x,t). \end{aligned} \tag{3.15}$$

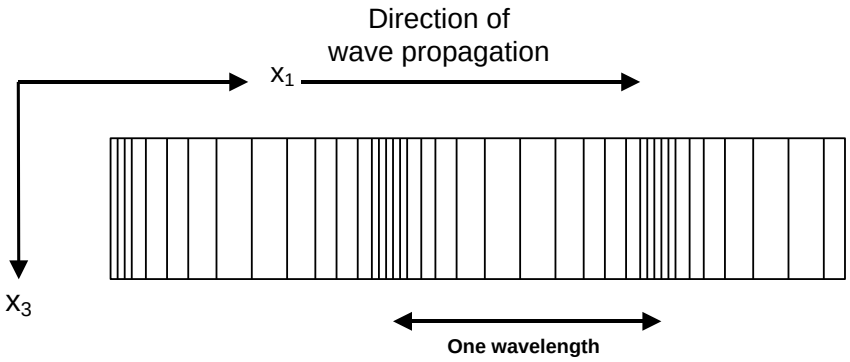

(a) Longitudinal wave

Fig. 3.3. Longitudinal and shear waves

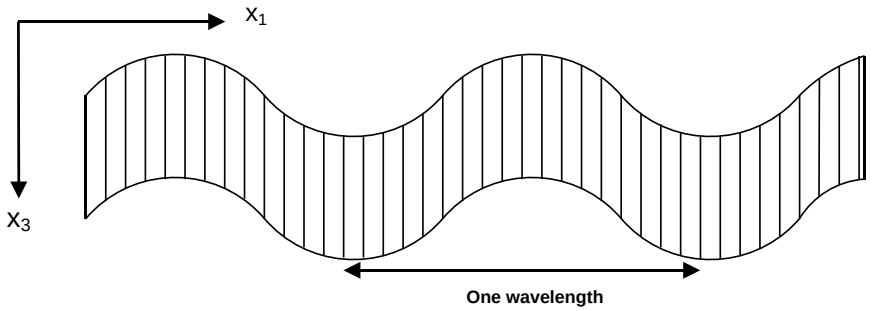

(b) Shear wave

Fig. 3.3. continued

Eq. (3.10) is difficult to solve using the displacement field described above. The longitudinal and shear components can be obtained using Helmholtz decomposition which uncouples the equations. For this purpose the displacements are expressed as a combination of a scalar potential ϕ and a vector potential $\boldsymbol{\psi}$.

$$\boldsymbol{u} = \nabla\phi + \nabla \mathbf{x}\, \boldsymbol{\psi}\,. \tag{3.16}$$

The uncoupled equations can be obtained by substituting Eq. (3.16) into Eq. (3.10)

$$\nabla^2\phi = \frac{1}{c_{\mathrm{L}}{}^2}\frac{\partial^2\phi}{\partial t^2}, \quad \text{and} \quad \nabla^2\boldsymbol{\psi} = \frac{1}{c_{\mathrm{S}}{}^2}\frac{\partial^2\boldsymbol{\psi}}{\partial t^2}, \tag{3.17}$$

where c_{L} and c_{S} are the longitudinal and shear wave speed, respectively. The expressions for the wave speeds are

$$c_{\mathrm{L}}{}^2 = \frac{\lambda + 2\mu}{\rho} = \frac{E(1-\upsilon)}{\rho(1+\upsilon)(1-2\upsilon)}, \tag{3.18}$$

$$c_{\mathrm{S}}{}^2 = \frac{\mu}{\rho} = \frac{E}{2\rho(1+\upsilon)}. \tag{3.19}$$

3.3.2. Rayleigh Waves

The existence of Rayleigh waves was predicted in 1885 by Lord Rayleigh. Rayleigh waves are surface waves that travel in a solid with boundaries introduced in

one of the three directions. In case of homogenous stress state, Rayleigh waves are nondispersive which means that the velocity of the wave does not change with the change in frequency. A Rayleigh wave propagates in the x_1- direction and attenuates exponentially in the x_3- direction. The displacement field for a Rayleigh wave can be described by

$$\begin{aligned} u_1 &= u_1\left(x_1, t\right), \\ u_2 &= 0, \\ u_3 &= u_3\left(\exp(x_3), t\right). \end{aligned} \tag{3.20}$$

The scalar and the vector potentials can be assumed to be of the form

$$\begin{aligned} \phi &= F(x_3)e^{ik(x_1-ct)}, \\ \psi &= G(x_3)e^{ik(x_1-ct)}, \end{aligned} \tag{3.21}$$

where G and F are functions of x_3, k is the wavelength and c is the wave speed. Substituting these into Eq. (3.17) yields the expressions that describe the surface wave motion

$$\begin{aligned} \phi &= Ae^{-\sqrt{k^2-k_{\mathrm{L}}{}^2}x_3}e^{ik(x_1-ct)}, \\ \psi &= Be^{-\sqrt{k^2-k_{\mathrm{S}}{}^2}x_3}e^{ik(x_1-ct)}, \end{aligned} \tag{3.22}$$

where k_{S} and k_{L} are the wavenumbers for the longitudinal and shear waves. The boundary conditions at the stress free surface are

$$T_{33}\left(x_3 = 0\right) = T_{13}\left(x_3 = 0\right) = 0. \tag{3.23}$$

Substituting the potentials into the boundary conditions results into the Rayleigh characteristic equation

$$\left(2 - \frac{c^2}{c_{\mathrm{S}}{}^2}\right)^4 - 16\left(1 - \frac{c^2}{c_{\mathrm{L}}{}^2}\right)\left(1 - \frac{c^2}{c_{\mathrm{S}}{}^2}\right) = 0. \tag{3.24}$$

Out of the six possible solutions, one satisfies the condition of a wave propagating in the x_1- direction and attenuating in the x_3- direction. Fig. 3.4 describes the propagation of Rayleigh waves. The Rayleigh wave exists for only a couple of wavelengths beneath the

surface as the energy dissipates very fast in the x_3-direction. At the surface, the particle motion is counterclockwise. At a depth of about 0.2 times the wavelength, the particle motion reverses direction since u_1 changes sign. This is shown in Fig. 3.4.

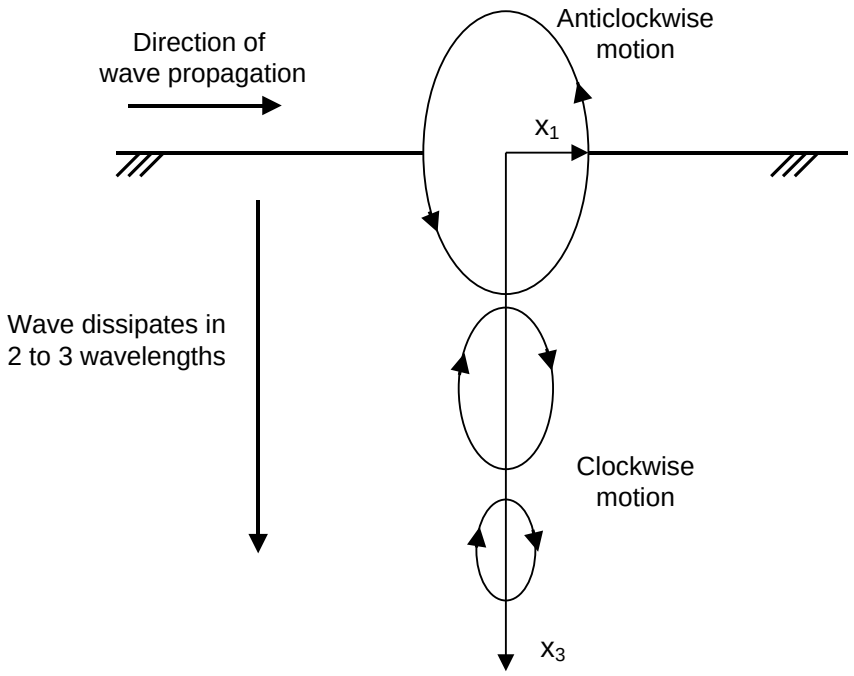

Fig. 3.4. Rayleigh wave propagation

3.3.3. Lamb Waves

3.3.3.1. Rayleigh-Lamb Equations

Lamb waves are named so in honor of the scientist Horace Lamb for his contribution to this subject matter. When a disturbance is generated in a thin plate such that the disturbance penetrates to the opposite surface then this produces a wave-guide effect. The disturbance travels as a guided wave consisting of compressions and rarefactions constrained between the two surfaces. If a Rayleigh wave is generated in a plate with a thickness equivalent to one wavelength, it degenerates to a Lamb wave. The

displacement field for a Lamb wave can be described by (Bedford and Drumheller, 1996)

$$u_1 = u_1(x_1, x_3, t),$$
$$u_2 = 0, \tag{3.25}$$
$$u_3 = u_3(x_1, x_3, t).$$

Substituting Eq. (3.21) in Eq. (3.17) and using the displacement field defined above gives the scalar and vector potentials

$$\phi = \left[A\sin\left(\sqrt{k^2 - k_{\mathrm{L}}{}^2}\, x_3\right) + B\cos\left(\sqrt{k^2 - k_{\mathrm{L}}{}^2}\, x_3\right)\right] e^{ik(x_1 - ct)}, \tag{3.26}$$

$$\psi = \left[C\sin\left(\sqrt{k^2 - k_{\mathrm{S}}{}^2}\, x_3\right) + D\cos\left(\sqrt{k^2 - k_{\mathrm{S}}{}^2}\, x_3\right)\right] e^{ik(x_1 - ct)}. \tag{3.27}$$

For a plate with thickness *h* the boundary conditions are

$$T_{33} = T_{13} = 0, \quad \text{at} \quad x_3 = \pm h/2. \tag{3.28}$$

Plugging in the boundary conditions in Eq. (3.26) and Eq. (3.27) gives the Rayleigh-Lamb equations.

For the symmetric mode this is given by

$$\frac{\tanh\left(\frac{h}{2}\sqrt{k^2 - k_{\mathrm{S}}{}^2}\right)}{\tanh\left(\frac{h}{2}\sqrt{k^2 - k_{\mathrm{L}}{}^2}\right)} = -\frac{4k^2\sqrt{k^2 - k_{\mathrm{S}}{}^2}\sqrt{k^2 - k_{\mathrm{L}}{}^2}}{\left(2k^2 - k_{\mathrm{S}}{}^2\right)^2}. \tag{3.29}$$

For the antisymmetric mode this is given by

$$\frac{\tanh\left(\frac{h}{2}\sqrt{k^2 - k_{\mathrm{S}}{}^2}\right)}{\tanh\left(\frac{h}{2}\sqrt{k^2 - k_{\mathrm{L}}{}^2}\right)} = -\frac{\left(2k^2 - k_{\mathrm{S}}{}^2\right)^2}{4k^2\sqrt{k^2 - k_{\mathrm{S}}{}^2}\sqrt{k^2 - k_{\mathrm{L}}{}^2}}. \tag{3.30}$$

3.3.3.2. Symmetric and Antisymmetric Lamb Modes

Particles moving in a plate can have a couple of configurations. In symmetric or '*extensional*' mode the particles vibrate symmetrically about the longitudinal axis of the plate. In antisymmetric mode, the particles vibrate antisymmetrically about the longitudinal axis. Fig. 3.5 shows the particle vibration in first mode for the symmetric and antisymmetric case as described by Hurlebaus (2005).

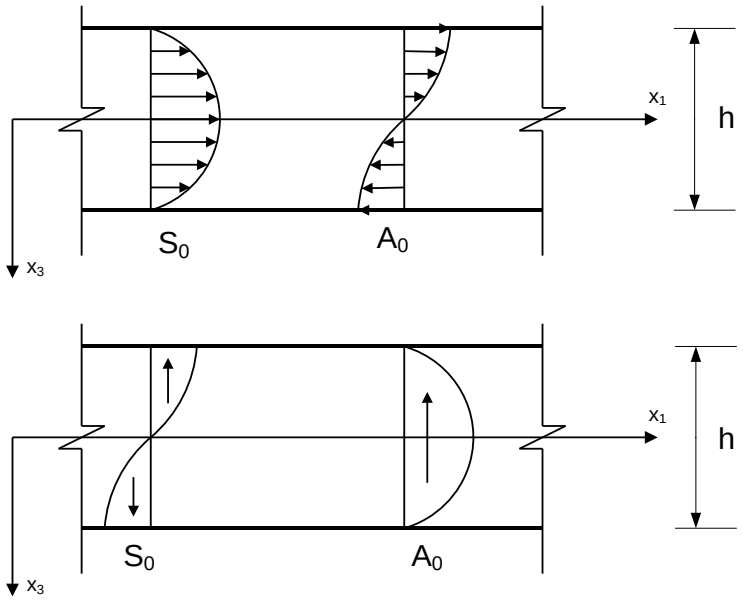

Fig. 3.5. Lamb wave modes showing displacements in x_1 and x_3-directions

Lamb waves are dispersive meaning that the propagating velocity of the Lamb wave is dependent on the frequency of the wave.

3.3.3.3. Phase and Group Velocity

Lamb waves exhibit a complicated behavior and the propagation of Lamb waves exhibits two velocities as described by Graff (1981). When two harmonic waves with the

same amplitude and slightly different frequencies interact, the resulting wave can be represented as

$$u = A\sin(k_1 x - \omega_1 t) + A\sin(k_2 x - \omega_2 t)\,. \tag{3.31}$$

$$u = 2A\cos\left(\frac{k_1 - k_2}{2}x - \frac{\omega_1 - \omega_2}{2}t\right)\sin\left(\frac{k_1 + k_2}{2}x - \frac{\omega_1 + \omega_2}{2}t\right)\,. \tag{3.32}$$

Eqn. (3.32) can be written as

$$u = D\sin\left(k_0 x - \omega_0 t\right), \tag{3.33}$$

$$D = 2A\cos(\Delta k x - \Delta\omega t)\,. \tag{3.34}$$

where, $k_0 = \frac{k_1 + k_2}{2}$, $\Delta k = \frac{k_1 - k_2}{2}$, $\Delta\omega = \frac{\omega_1 - \omega_2}{2}$, and $\omega_0 = \frac{\omega_1 + \omega_2}{2}$.

Thus, the carrier wave propagates with its amplitude modulated by *D*. The modulation *D* changes slowly and builds up a wave group. The velocity of the carrier is referred to as the phase velocity c_p and the velocity at which the over-all wave group propagates is referred to as group velocity c_g. The two velocities are

$$c_p = \frac{\omega_0}{k_0}, \qquad \text{and} \tag{3.35}$$

$$c_g = \frac{\Delta\omega}{\Delta k} = \frac{\mathrm{d}\omega}{\mathrm{d}k}\,. \tag{3.36}$$

CHAPTER IV

ANALYTICAL MODEL

A general analytical model that describes the acoustoelastic effect of ultrasonic waves is discussed in this chapter. This model describes the fundamental approach for obtaining the relationship between wave speed and stress or polarization and stress for the ultrasonic waves under consideration for this research. Further, three individual models are elaborated, one for longitudinal and shear waves, next for Rayleigh waves and another one for Lamb waves.

4.1. Wave Motion in a Prestressed Body

4.1.1. Stresses and Displacements

The material properties like material density, Young's modulus etc. are defined with respect to the natural state of the body. In order to establish the nonlinearity due to large deformations the theory of acoustoelasticity takes into account the third order elastic constants.

The stress state at a given point can be defined in two ways. In the initial state the Cauchy stress tensor t^i_{JK} defines the force per unit predeformed area with an outward normal $\boldsymbol{N}$ (see Fig. 3.2). The Piola-Kirchhoff stress tensor $T^i_{\alpha\beta}$ refers to the stress at the same point but in the natural configuration. The relation between the two is given by

$$t^i_{JK} = \frac{1}{\partial X/\partial \xi}\frac{\partial X_K}{\partial \xi_\beta}\frac{\partial X_J}{\partial \xi_\alpha}T^i_{\alpha\beta} \ . \tag{4.1}$$

Using the same analogy the relation between Cauchy stress tensor t^f_{ij} referring to the final state and the Piola-Kirchhoff stress tensor $T^f_{\alpha\beta}$ referring to the natural configuration is

$$t_{ij}^{f} = \frac{1}{\partial x/\partial \xi}\frac{\partial x_i}{\partial \xi_\alpha}\frac{\partial x_j}{\partial \xi_\beta}T_{\alpha\beta}^{f}. \tag{4.2}$$

When any dynamic disturbance such as an ultrasonic wave is superimposed on a predeformed body, there is a stress change from the initial to the final state. In terms of Piola-Kirchhoff stress it follows that

$$\begin{aligned} \boldsymbol{T} &= \boldsymbol{T}^{f} - \boldsymbol{T}^{i}, \\ T_{JK} &= T_{JK}^{f} - t_{JK}^{i}, \\ T_{\alpha\beta} &= T_{\alpha\beta}^{f} - T_{\alpha\beta}^{i}. \end{aligned} \tag{4.3}$$

4.1.2. Equation of Motion for a Prestressed Body

For a body having a volume *V*, surface area *A*, density ρ, and with a final stress given by the Piola-Kirchhoff tensor in the final state T_{KJ}^{f}, the equations of motion are expressed by (Pao et al., 1984)

$$\frac{\partial}{\partial X_K}\left(T_{KJ}^{f} + T_{KL}^{f}\frac{\partial u_J}{\partial X_L}\right) = \rho^{i}\frac{\partial^2 u_J}{\partial t^2}. \tag{4.4}$$

The deformation from the natural to initial state is static and hence it must satisfy the equilibrium equation

$$\frac{\partial t_{IK}^{i}}{\partial X_K} = 0. \tag{4.5}$$

Subtracting Eq. (4.5) from Eq. (4.4) gives the equation for the incremental stress and incremental displacement *u*

$$\frac{\partial}{\partial X_I}\left(T_{IJ} + t_{IK}^{i}\frac{\partial u_J}{\partial x_K}\right) = \rho\frac{\partial^2 u_J}{\partial t^2}. \tag{4.6}$$

The incremental stress T_{IJ} can be replaced by a stress strain relationship as given by Hooke's law. Pao et al. (1984) provides a complete derivation of this relationship where they introduce the TOE constants

$$T_{IJ} = C_{IJKL} \frac{\partial u_K}{\partial X_L}. \tag{4.7}$$

The relation between mass densities, ρ^i and ρ^o in the initial and natural states respectively, can be approximated as

$$\rho^i = \rho^o \left(1 - \varepsilon^i_{NN}\right). \tag{4.8}$$

It follows from Eq. (4.6), Eq. (4.7) and Eq. (4.8) that

$$(C_{IJKL} + \delta_{JK} t^i_{IL}) \frac{\partial^2 u_K}{\partial x_I \partial x_L} = \rho^0 (1 - \varepsilon^i{}_{NN}) \frac{\partial^2 u_J}{\partial t^2}. \tag{4.9}$$

4.1.3. Solution for a Plane Wave

The solution for the displacement *u* for a plane-wave is of the form

$$u_j = b_j \left(P_d\right)_j \mathrm{e}^{ik(x_1 - ct)}, \tag{4.10}$$

where b_j is the displacement field and P_d is the decay parameter. The time derivative of the displacement equation can be expressed as

$$\ddot{u}_j = -k^2 c^2 u_j = -\omega^2 u_j. \tag{4.11}$$

Using tensor analysis, it can be proved that $\frac{\partial^2 u_K}{\partial x_I \partial x_L} = k_I k_L u_K$ (Rose, 2004). Using this expression and Eq. (4.11) the equation of motion can be written as

$$(C_{IJKL} + \delta_{JK} t^i_{IL}) k_I k_L u_K = \rho^i \omega^2 u_J. \tag{4.12}$$

Applying $u_J = u_K \delta_{JK}$ and replacing ρ^i by ρ for ease in writing, the above equation can be written as

$$\left((C_{IJKL} + \delta_{JK} T_{IL}) k_I k_L - \rho \omega^2 \delta_{JK}\right) u_K = 0, \tag{4.13}$$

$$\left|\lambda_{JK} - \rho \omega^2 \delta_{JK}\right| = 0, \tag{4.14}$$

where the Christoffel acoustic tensor is defined as

$$\lambda_{JK} = (C_{IJKL} + \delta_{JK} T_{IL}) k_I k_L. \tag{4.15}$$

Thus, Eq. (4.13) can be written as

$$\left[\boldsymbol{A}\right]\left\{\boldsymbol{b}\right\}=0, \tag{4.16}$$

which is the Christoffel equation.

In order to determine the displacement field b_j, the determinant of the coefficient matrix $\boldsymbol{A}$ must be equal to zero. Then, solving Eq. (4.16) for the eigenvectors leads to the displacement fields. Inserting the wave solution Eq. (4.10) into the boundary conditions specific to a wave leads to the equations of the form

$$\left[\boldsymbol{D}\right]\left\{\boldsymbol{U}\right\}=0. \tag{4.17}$$

The condition for the nontrivial solution is that

$$\left\|\boldsymbol{D}\right\|=0. \tag{4.18}$$

For Rayleigh waves, Eq. (4.18) yields the Rayleigh wave speed c_{R} and the decay parameter p for a stress of T_{11}. For Lamb waves this equation yields the frequency ω and wavenumber k. The next part of this section describes the analytical models specific to the ultrasonic waves under consideration.

4.2. Longitudinal and Shear Waves

To obtain an analytical solution of the longitudinal and shear wave velocities, the model pointed out by Egle and Bray (1976) is followed. They describe the expressions for wave speeds as derived by Hughes and Kelly (1953) using Murnaghan's (1951) theory of finite deformations. The wave speeds for a plane wave propagating in x_1-direction and having displacements in x_1, x_2 and x_3-directions are obtained by,

$$c_L=v_{11}=\sqrt{\frac{(\lambda+2\mu+(2l+\lambda)\varepsilon_{NN}+(4m+4\lambda+10\mu)\varepsilon_{11}}{\rho}}\ , \tag{4.19}$$

$$c_S=v_{12}=\sqrt{\frac{\mu+\left(4\mu+\nu(n/2)+m(1-2\nu)\right)\varepsilon_{11}}{\rho}}\quad , \tag{4.20}$$

$$v_{22} = \sqrt{\frac{\lambda + 2\mu + \left(2l(1-2\nu) - 4\nu(m+\lambda+2\mu)\right)\varepsilon_{11}}{\rho}}\,, \tag{4.21}$$

$$v_{21} = \sqrt{\frac{\mu + \left((\lambda+2\mu+m)(1-2\nu) + n\nu/2\right)\varepsilon_{11}}{\rho}}\,, \tag{4.22}$$

$$v_{23} = \sqrt{\frac{\mu + \left((\lambda+m)(1-2\nu) - 6\nu\mu - n/2\right)\varepsilon_{11}}{\rho}}\,, \tag{4.23}$$

where *l*, *m*, and *n* are the third order elastic constants (Egle and Bray, 1976), v_{ij} is the wave speed of a wave traveling in the *i*-direction and with particle vibration in *j*-direction.

4.3. Lamb Waves

4.3.1. Solution of the Christoffel Equation

Section 4.1 introduced the basic idea for determining the wave speed of an ultrasonic wave using the theory discussed in Chapter III. This section develops a model to predict the wave speed of Lamb waves in particular. This analysis follows the model described by Desmet et al. (1996). This model, however, neglects the effect of the TOE constants.

The plane wave solution for displacement for a Lamb wave can be expressed by taking $\left(P_d\right)_j = 1$ in Eq. (4.10). This gives

$$u_j = b_j \mathrm{e}^{ik(x_1 - ct)}.$$

The Christoffel acoustic tensor can be determined using Eq. (4.15). More details on this topic can be obtained from (Rose, 2004). Since only the longitudinal forces in the rail are of concern, a uniaxial stress $T_{11} = T$ in the x_1 - direction is assumed and all other stresses are neglected. Thus, the acoustic tensor matrix $\boldsymbol{A}$ is determined to be (Desmet et al., 1996)

$$A_{11} = \left(\frac{\pi}{h}\right)^2 \left((C_{11}+T)K_1 + \frac{(C_{11}-C_{12})(K_3-W)}{2}\right), \tag{4.24}$$

$$A_{22}=\left(\frac{\pi}{h}\right)^2\left[\frac{(C_{11}-C_{12})}{2}\left(K_1+\frac{(K_3-W)}{2}\right)+TK_1\right], \tag{4.25}$$

$$A_{33}=\left(\frac{\pi}{h}\right)^2\left(\frac{(C_{11}-C_{12})(K_1-W)}{2}+TK_1+C_{11}K_3\right), \tag{4.26}$$

$$A_{13}=\left(\frac{\pi}{h}\right)^2\frac{(C_{11}+C_{12})}{2}\sqrt{K_1K_3}\,, \tag{4.27}$$

$$A_{31}=A_{13}, \tag{4.28}$$

$$A_{12}=A_{23}=A_{21}=A_{32}=0, \tag{4.29}$$

where the dimensionless quantities K_1, $\boldsymbol{K_3}$ and W (Desmet et al., 1996) are

$$K_1=\left(\frac{h}{\pi}k\right)^2,\quad K_3=\left(\frac{h}{\pi}k_3\right)^2,\quad W=\left(\frac{h}{\pi}\right)^2\left(\frac{2\rho\omega^2}{C_{11}-C_{12}}\right). \tag{4.30}$$

The matrix $\boldsymbol{A}$ is a function of the circular frequency and wavenumber. Eq. (4.16) has a solution when the determinant of the matrix $\boldsymbol{A}$ goes to zero. Using the above expressions for A_{ij}'s gives

$$A_{22}\left(A_{11}A_{33}-A_{13}^2\right)=0. \tag{4.31}$$

The solution for $A_{22}=0$ gives the shear horizontal mode and is not discussed here. The solution for $\left(A_{11}A_{33}-A_{13}^2\right)=0$ is given by

$$(K_3)_{2,3}=\left(-b\pm\sqrt{b^2-4ac}\right)/2a, \tag{4.32}$$

where

$$a=C_{11}\frac{C_{11}-C_{12}}{2},$$

$$b=\left[(C_{11}+T)C_{11}-C_{12}^2\right]K_1+\left[\left(T-2C_{12}\right)K_1-\frac{3C_{11}-C_{12}}{2}W\right]\frac{C_{11}-C_{12}}{2},$$

$$c = (C_{11} + T)(X + T)K_1^2\left[-\left(\frac{3C_{11} - C_{12}}{2} + 2T\right)K_1 W + \frac{C_{11} - C_{12}}{2}W^2\right]\frac{C_{11} - C_{12}}{2}.$$

Solving for the null-space of ***A***, the displacement fields b_j are obtained as

$$b_1 = \pm\sqrt{K_1 R_p}\,\boldsymbol{U_p}\,\frac{C_{11} + C_{12}}{2}, \tag{4.33}$$

$$b_2 = 0, \tag{4.34}$$

$$b_3 = -\boldsymbol{U_p}\left((C_{11} + T)K_1 + \frac{C_{11} - C_{12}}{2}(R_p - W)\right), \tag{4.35}$$

with $p = 1, 2, 3, 4$ where $\boldsymbol{R_{1,2}} = \boldsymbol{(K_3)_2}$, and $\boldsymbol{R_{3,4}} = \boldsymbol{(K_3)_3}$.

4.3.2. Boundary Conditions

The boundary conditions for Lamb waves are

$$\sigma_{33} = \sigma_{13} = 0 \text{ at } x_3 = \pm h/2, \tag{4.36}$$

for a Lamb wave propagating through a plate of thickness *h*. Eq. (4.36) can be written with the help of Hooke's law as

$$\sigma_{I3} = C_{I3KL}\frac{\partial u_K}{\partial X_L} = 0. \tag{4.37}$$

The displacement field ***b*** for each value of $p = 1..4$ can be obtained and hence the displacement can be written as a linear combination in the matrix notation as

$$\boldsymbol{u} = \boldsymbol{B}\boldsymbol{f}e^{ik(x_1 - ct)}, \tag{4.38}$$

with the vector ***f*** giving the factors for the linear combination, and

$$\boldsymbol{B} = \left[\boldsymbol{b_1}, \boldsymbol{b_2}, \boldsymbol{b_3}, \boldsymbol{b_4}\right]. \tag{4.39}$$

Inserting the plane wave solution Eq. (4.38) in the boundary conditions Eq. (4.37) yields final condition as given by Eq. (4.17). The matrix ***D*** is a function of the circular frequency and wavenumber. As explained earlier, in Lamb waves, two types of particle vibrations are possible, namely, symmetric and antisymmetric. In order to obtain the nontrivial solution, Eq. (4.18) must be satisfied. Desmet et al. (1996) gives the conditions for the two cases.

For the symmetric case,

$$\begin{aligned} &\boldsymbol{D_1(R_1)D_2(R_2)}\sin\left(\sqrt{R_1}\frac{\pi}{2}\right)\cos\left(\sqrt{R_3}\frac{\pi}{2}\right)- \\ &\boldsymbol{D_1(R_3)D_2(R_1)}\sin\left(\sqrt{R_3}\frac{\pi}{2}\right)\cos\left(\sqrt{R_1}\frac{\pi}{2}\right)=0 \end{aligned}, \tag{4.40}$$

and for the antisymmetric case,

$$\begin{aligned} &\boldsymbol{D_1(R_1)D_2(R_2)}\cos\left(\sqrt{R_1}\frac{\pi}{2}\right)\sin\left(\sqrt{R_3}\frac{\pi}{2}\right)- \\ &\boldsymbol{D_1(R_3)D_2(R_1)}\cos\left(\sqrt{R_3}\frac{\pi}{2}\right)\sin\left(\sqrt{R_1}\frac{\pi}{2}\right)=0 \end{aligned}, \tag{4.41}$$

where

$$\boldsymbol{D_1(R)} = C_{12}R + \frac{C_{11}-C_{12}}{2}W - (C_{11}+T)K_1,$$

$$\boldsymbol{D_2(R)} = \sqrt{R}\left[C_{12}\frac{C_{11}+C_{12}}{2} - C_{11}\left((C_{11}+T)K_1 + \frac{C_{11}-C_{12}}{2}(W-R)\right)\right].$$

Equations (4.40) an (4.41) give the dispersion relations for the symmetric and antisymmetric Lamb modes, respectively. Solving these equations gives the wavenumber and circular frequency for the Lamb modes. Using these relations one can plot the Lamb modes in the (k,ω) plane. The phase velocity c_p and the group velocity c_g for the wave are determined using the following relations

$$c_p = \frac{\omega}{k}, \tag{4.42}$$

$$c_g = \frac{\mathrm{d}\omega}{\mathrm{d}k}, \tag{4.43}$$

where ω is the angular frequency and k is the wavenumber.

4.4. Rayleigh Waves

4.4.1. Solution of the Christoffel Equation

Eq. (4.10) for a Rayleigh wave can be expressed by taking $\left(P_d\right)_j = e^{ipkx_3}$, since the Rayleigh wave decays in the x_3 - direction. The wave solution then becomes

$$u_j = b_j e^{ik(x_1 + px_3 - ct)}. \tag{4. 44}$$

By plugging in Eq. (4.44) into Eq. (4.9) it follows that (Junge, 2003)

$$\begin{bmatrix} \delta_{IK} t^i_{22} + \hat{C}_{I2K2}) p^2 + (\delta_{IK} t^i_{12} + \hat{C}_{I1K2} + \delta_{IK} t^i_{21} + \hat{C}_{I2K1}) p \\ +(\delta_{IK} t^i_{11} + \hat{C}_{I1K1}) - \delta_{IK} \rho_0 (1 - \varepsilon^i_{NN}) c_{\mathrm{R}}{}^2 \end{bmatrix} \boldsymbol{u} = 0. \tag{4.45}$$

Since the stress is a uniaxial stress in the x_1 - direction this equation reduces to Eq. (4.16) in the following form

$$[\boldsymbol{A}]\{\boldsymbol{b}\} = \left\{ p^2 \hat{\boldsymbol{S}} + p(\hat{\boldsymbol{R}} + \hat{\boldsymbol{R}}^T) + \hat{\boldsymbol{Q}} - \rho_0 (1 - \varepsilon^i{}_{NN}) c_{\mathrm{R}}{}^2 \boldsymbol{I} \right\} \boldsymbol{b} = 0, \tag{4.46}$$

where the three matrices $\boldsymbol{S}$, $\boldsymbol{R}$ and $\boldsymbol{Q}$ are defined as

$$\hat{\boldsymbol{S}} = C_{I2K2}, \quad \hat{\boldsymbol{R}} = C_{I1K2}, \quad \hat{\boldsymbol{Q}} = C_{I1K1} + \delta_{IK} T^i{}_{11}.$$

The matrix $\boldsymbol{I}$ is the identity matrix. $\boldsymbol{A}$ is a function of the Rayleigh wave speed and the decay parameter p.

Solving for the nontrivial solution of Eq. (4.46) yields three pairs of complex conjugate roots for p. The displacement field $\boldsymbol{b}$ can be solved for each value of p_i by solving for the null vector of $\boldsymbol{A}$. Once the b_j*'s* are determined one can express the displacement as a linear combination of the single solutions using the matrix notation as shown in Eq. (4.47).

$$\boldsymbol{u} = \boldsymbol{B}\boldsymbol{P}_{\boldsymbol{d}} \boldsymbol{f} e^{ik(x_1 - ct)}, \tag{4.47}$$

with the vector $\boldsymbol{f}$ giving the factors for the linear combination,

$$\boldsymbol{B} = [\boldsymbol{b_1}, \boldsymbol{b_2}, \boldsymbol{b_3}], \tag{4.48}$$

and

$$\boldsymbol{P}_{\boldsymbol{d}} = \begin{pmatrix} \mathrm{e}^{i(kp_1 x_3)} & 0 & 0 \\ 0 & \mathrm{e}^{i(kp_2 x_3)} & 0 \\ 0 & 0 & \mathrm{e}^{i(kp_3 x_3)} \end{pmatrix}. \tag{4.49}$$

4.4.2. Boundary Conditions

The boundary conditions for a Rayleigh wave propagating in the x_1-direction and decaying in the x_3- direction are

$$\sigma_{33} = \sigma_{13} = 0 \text{ at } x_3 = 0 . \tag{4.50}$$

Using Hooke's law and plugging in Eq. (4.47) into the boundary conditions yields Eq. (4.17) in the form

$$[\boldsymbol{D}]\{\boldsymbol{f}\} = (\hat{\boldsymbol{R}}^{\boldsymbol{T}}\boldsymbol{B} + \hat{\boldsymbol{S}}\boldsymbol{B}\boldsymbol{P})\boldsymbol{f} = 0 , \tag{4.51}$$

with

$$\boldsymbol{P} = \begin{bmatrix} p_1 & 0 & 0 \\ 0 & p_2 & 0 \\ 0 & 0 & p_3 \end{bmatrix}.$$

The value of c_R obtained that satisfies both the Equations (4.46) and (4.49) is the wave speed of the Rayleigh wave at a uniaxial stress *T*. The vector $\boldsymbol{f}$ is obtained by solving for the null-space of $\boldsymbol{D}$. The displacements are thus determined by using Eq. (4.47). Since Rayleigh wave has maximum amplitude at the surface $(x_3 = 0)$, the displacement at the surface is given by

$$\boldsymbol{u} = \boldsymbol{B}\boldsymbol{f}e^{ik(x_1 - ct)} . \tag{4.52}$$

The polarization Π, of a Rayleigh wave is defined as the ratio of maximum in-plane, to the maximum out-of-plane displacement of a particle on the free surface. The polarization vector is given by

$$\vec{\Pi} = \boldsymbol{B}\boldsymbol{f} \ . \tag{4.53}$$

At the surface, $x_3 = 0$; the polarization of the Rayleigh wave is given as

$$\Pi = \frac{(\boldsymbol{B}\boldsymbol{f})_1}{(\boldsymbol{B}\boldsymbol{f})_3} . \tag{4.54}$$

CHAPTER V

NUMERICAL SIMULATION

The theory of acoustoelasticity has been explained in the previous chapters. This section applies this theory in order to provide a numerical solution to the propagation of ultrasonic waves through rail steel. Firstly, the generic algorithms followed to obtain a numerical solution are discussed. This is followed by the simulation results. The acoustoelasticity of various ultrasonic waves is compared. Finally, important conclusions regarding the numerical solution are presented.

5.1. Generic Algorithms for Numerical Simulation

The algorithms are easy to implement in any programming tool. For this research, MATLAB was used to program the algorithms.

5.1.1. Rayleigh Wave

The objective of this problem is to determine the Rayleigh wave speed c_{R} and polarization Π for a material under constant stress. The algorithm proceeds in the steps as described below following Junge (2003)

STEP 1. Make an initial guess for the wave speed using the equation given by Graff (1978)

$$c_{\mathrm{R}0} = \frac{0.87 + 1.12\upsilon}{1+\upsilon} c_{\mathrm{S}0}, \tag{5.1}$$

where, the subscript '0' denotes zero stress and υ is Poisson's ratio.

STEP 2. Using the wave speed obtained from Eq. (5.1), compute p_i that satisfies Eq. (4.40), or in other words, makes the determinant of $\boldsymbol{A}$ equal to zero.

STEP 3. For each value of *p*, compute the null-space $\boldsymbol{b}$ of Eq. (4.41).

STEP 4. Construct the matrix $\boldsymbol{D}$ as per Eq. (4.46).

STEP 5. Check for the determinant of ***D***.

- If the determinant is equal to zero then the assumed value of c_R is correct. Proceed to STEP 6.
- If the determinant is not equal to zero then, change the value of c_R and repeat steps 2, 3, 4 and 5.

STEP 6. Use this value of c_R to determine the vector ***f*** which is the null-space of ***D***.

STEP 7. Compute the polarization using Eq. (4.49).

5.1.2. Lamb Waves

The objective of this problem is to determine the wavenumber *k* and circular frequency ω of the propagating wave in order to plot the dispersion relations. The basic principle is to iteratively find the ω-k pairs for each mode. The algorithm proceeds in the steps as described below following Lowe (1992)

STEP 1. Make an initial assumption of the wavenumber *k* and frequency ω.

STEP 2. With the physical properties of rail steel set up Eq. (4.35) and Eq. (4.36) with the unknowns *k* and ω.

STEP 3. In this step a coarse search is made by evaluating the functions in Eq. (4.35) (or Eq. (4.36)) for a fixed value of wavenumber and over a range of values on the frequency axis. Observing the values of the function that crosses zero gives the approximate location of a Lamb mode. This search gives all possible modes that could be obtained starting from an assumed wavenumber.

STEP 4. Select an approximate location found in STEP 3, determine the exact location by using a numerical technique such as Regula Falsi method that converges to the point where zero exists. This gives the first pair (k_1, ω_1) on the curve.

STEP 5. Increase *k* by a small amount Δk, and repeat step 3 and 4 to find another pair (k_2, ω_2).

STEP 6. Determine the slope of the line joining the two points.

STEP 7. Increase k_2 by another Δk and using the slope found in step 6 extrapolate to the value of ω_3.

STEP 8. To determine accurately the value of ω_3, once again Regula Falsi method is employed to converge to a root between $\omega_3 + \Delta\omega$ and $\omega_3 - \Delta\omega$ where $\Delta\omega$ is a small arbitrary increment. This gives a third point.

STEP 9. Repeat the steps 7 and 8 determining the (k, ω) pairs each time. The iterations are stopped when the desired value of frequency is reached.

STEP 10. For the next mode go to STEP 3 and start with another approximate location. Repeat STEPS 4 through 9 to determine another curve.

STEP 11. Plot ω versus *k* for various modes obtained.

The above algorithm generates the dispersion curves for Lamb modes.

5.2. Sensitivity Constants

The numerical simulation was carried out for different stresses ranging from a compression of T_{11} = -400 MPa to a tension of T_{11} = + 400 MPa. A lot of literatures define the sensitivity constants as a relative change in wave speed and polarization per unit change in stress. This is due to the fact that the absolute change in wave speed or polarization with stress is very small.

The relative change in wave speed is defined as

$$\Delta c = \frac{c - c_0}{c_0}. \tag{5.2}$$

The relative change in polarization is defined as

$$\Delta\Pi = \frac{\Pi - \Pi_0}{\Pi_0}, \tag{5.3}$$

where c is the wave speed, Π is the polarization and the subscript '0' indicates these parameters at zero stress. Using these relations, the sensitivity constants for wave speed and polarization are respectively defined as

$$k_c = \frac{\Delta c}{\Delta \sigma}, \tag{5.4}$$

$$k_p = \frac{\Delta \Pi}{\Delta \sigma}. \tag{5.5}$$

5.3. Simulation Results

This research focuses on the effect of a uniaxial stress T_{11} in the propagation direction x_1 on the wave speed of various ultrasonic waves and polarization of Rayleigh waves. In addition, the effect of variations in TOE constants on sensitivity constants of Rayleigh waves is also discussed.

Analytical models as discussed earlier were encoded in MATLAB. Rail steel has yield strength of 450 MPa. The model is run for stresses varying between ± 400 MPa where '+' indicates tension and '-' indicates compression. The elastic properties of rail steel used for this analysis are taken from Junge (2003) and are presented in Table 5.1.

Table 5.1. Density, Lamé constants and TOE constants for rail steel

ρ [kg/m^3]	λ [GPa]	μ [GPa]	υ_1 [GPa]	υ_2 [GPa]	υ_3 [GPa]
7800	115.8	79.9	36	-266	178.5

5.3.1. Rayleigh Waves

The simulation results are shown in Tables 5.2 and 5.3. Fig. 5.1 shows the relative change in polarization for a uniaxial stress variation from -400 MPa to +400 MPa. It is observed that the Rayleigh wave speed increases with increasing tension and decreases with increasing compression. Also, it is observed that polarization decreases with increasing tension and decreases with increasing compression. Both the

relationships are linear which is consistent with the observations of Egle and Bray (1976) and Hirao et al. (1981). This relationship can be expressed in terms of the sensitivity constants k_c and k_p. For rail steel these constants are

$$k_c = 1.508 \times 10^{-5} / \text{MPa} \text{ and,}$$

$$k_p = -9.011 \times 10^{-6} / \text{MPa} .$$

It is found that for other materials such as aluminum, as investigated by Junge et al. (2004), and mild steel, investigated by Hirao et al. (1981), this relationship is opposite to that observed in rail steel. Comparing the TOE constants for different materials from Junge (2003) it is observed that the sensitivity constants for wave speed k_c and polarization k_p depend on the TOE constants.

Table 5.2. Comparison of sensitivity constants for different materials

Material	v_1 [GPa]	v_2 [GPa]	v_3 [GPa]	k_c [1/MPa]	k_p [1/MPa]
Mild Steel	-13	-200	-200	-5.72×10^{-7}	9.182×10^{-6}
Aluminum	-27.7	-91.7	-89.3	-2.88×10^{-6}	2.789×10^{-5}
Rail Steel	36	-266	178.5	1.508×10^{-5}	-9.011×10^{-6}

Table 5.3. Simulation results showing the change in Rayleigh wave speed and polarization

T_{11} [MPa]	c_R [m/s]	Polarization Vector		Δc_R	$\Delta\Pi$
		u_1	u_3		
-400	2948.27	0.551287	0.834316	-6.033E-03	3.622E-03
-300	2952.76	0.550939	0.834546	-4.521E-03	2.711E-03
-200	2957.23	0.550591	0.834775	-3.012E-03	1.803E-03
-100	2961.70	0.550245	0.835003	-1.505E-03	8.996E-04
0	2966.17	0.549900	0.835230	0.000E+00	0.000E+00
100	2970.62	0.549556	0.835457	1.502E-03	-8.957E-04
200	2975.07	0.549214	0.835682	3.002E-03	-1.788E-03
300	2979.51	0.548872	0.835906	4.500E-03	-2.676E-03
400	2983.95	0.548532	0.836130	5.995E-03	-3.561E-03

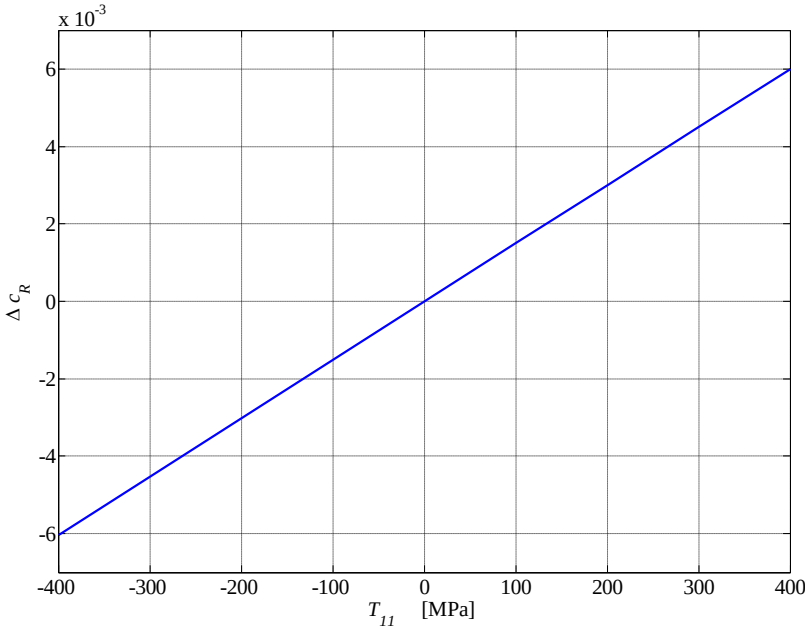

(a) Relative change of wave speed

Fig. 5.1. Relative change in Rayleigh wave speed and polarization for uniaxial stress change along propagation direction

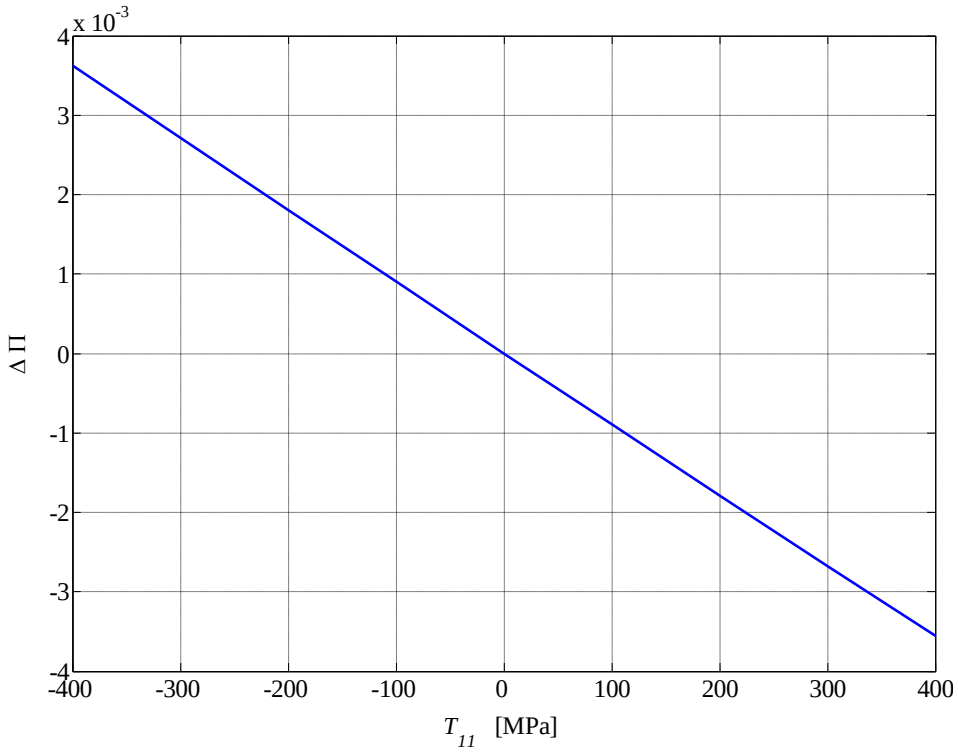

(b) Relative change of polarization

Fig. 5.1. continued

Fig. 5.2 shows the motion of a particle on the surface of rail steel. The polarization of Rayleigh waves is the ratio of the maximum in-plane to the maximum out-of-plane displacements. The change in polarization with stress is visualized from the two ellipses in the figure that indicate the motion of the particle when the stress changes from 0 MPa to -10 GPa. It may be noted that this model does not take into account the fact that yield stress of steel is 450 MPa. Fig. 5.2 is only for demonstrating the effect of stress change on the polarization ellipse.

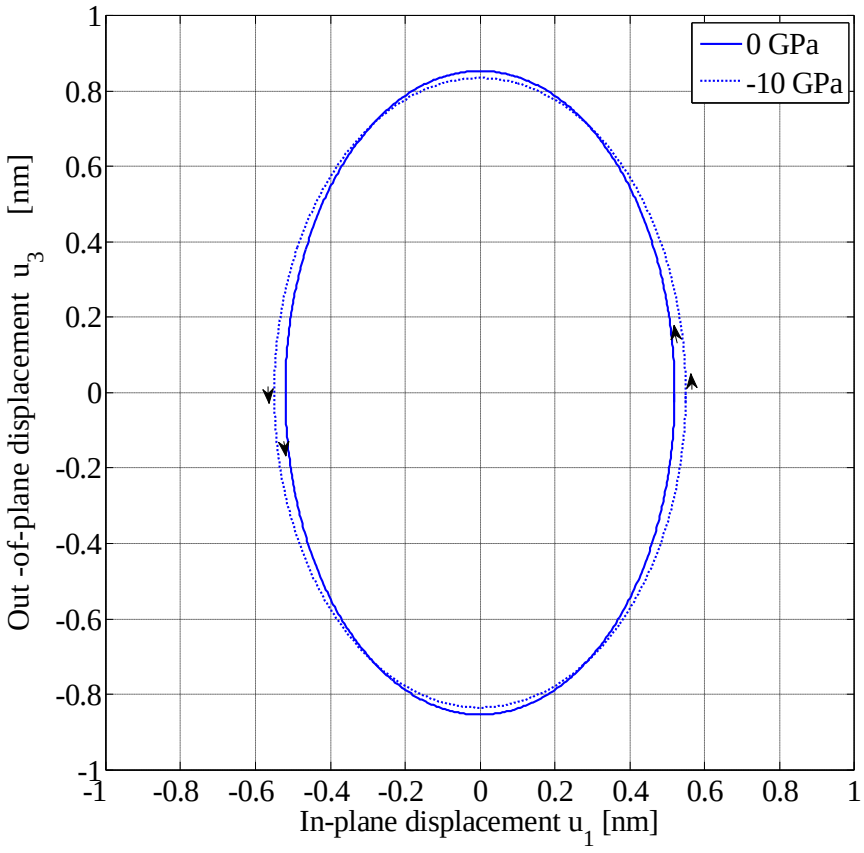

Fig. 5.2. Rayleigh wave polarization

5.3.2. Sensitivity of TOE Constants – Rayleigh Waves

The simulation assumes that the TOE constants remain unchanged throughout the simulation. The experiments by Egle and Bray (1976) on two rail samples reveal a maximum variation of 4.1%. In order to evaluate the dependency of sensitivity constants on variation in TOE constants, a simulation is carried out. This simulation assumes a scatter of ± 10 %. On the other hand, Lamé constants can be accurately determined and hence their values are assumed to be constant. Table 5.4 shows the variation in TOE constants used in the analysis.

Table 5.4. Variation of TOE constants-Rayleigh Waves [GPa]

	Min. (-10%)	Average	Max. (+10%)
υ_1	32.4	36	39.6
υ_2	-292.6	-266	-239.4
υ_3	160.65	178.5	196.35

Fig. 5.3 shows the results for the sensitivity analysis. From the two plots, it is evident that the scatter in Rayleigh wave speed is less as compared to the scatter in wave polarization. This means that the variability in TOE constants has more effect on wave polarization. Table 5.5 shows the influence of TOE constants on the sensitivity constants. Change in k_p is approximately three times the change in k_c.

Table 5.5. Variation in sensitivity constants-Rayleigh Waves

	k_c [1/MPa]	Δk_c %	k_p [1/MPa]	Δk_p %
Max.	1.619E-05	7.72	-1.082E-05	20.10
Avg.	1.503E-05	0.000	-9.011E-06	0.000
Min.	1.387E-05	-7.72	-7.112E-06	-21.08

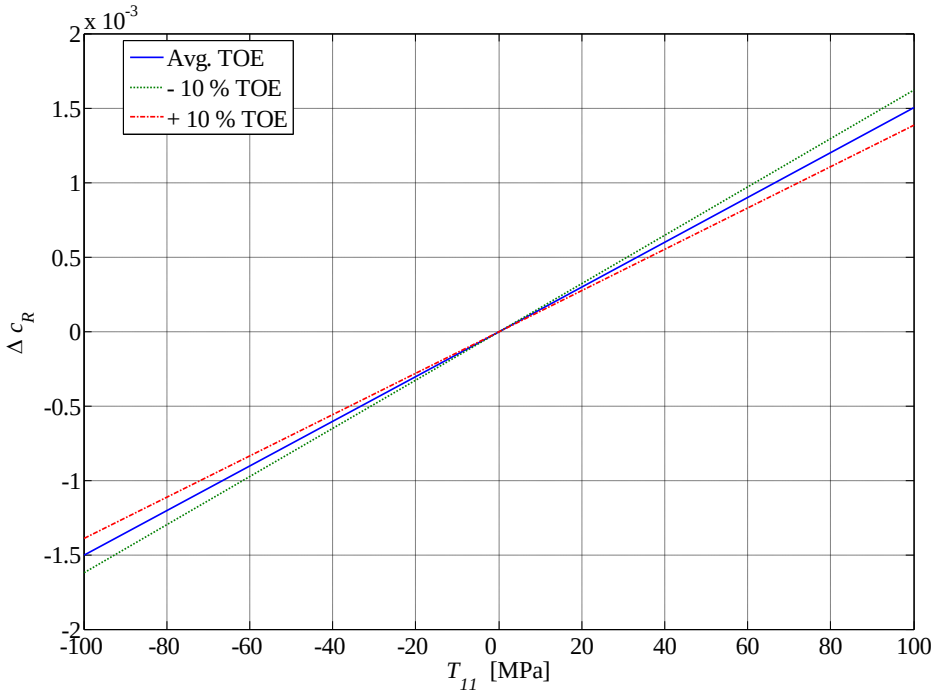

(a) Relative change in wave speed.

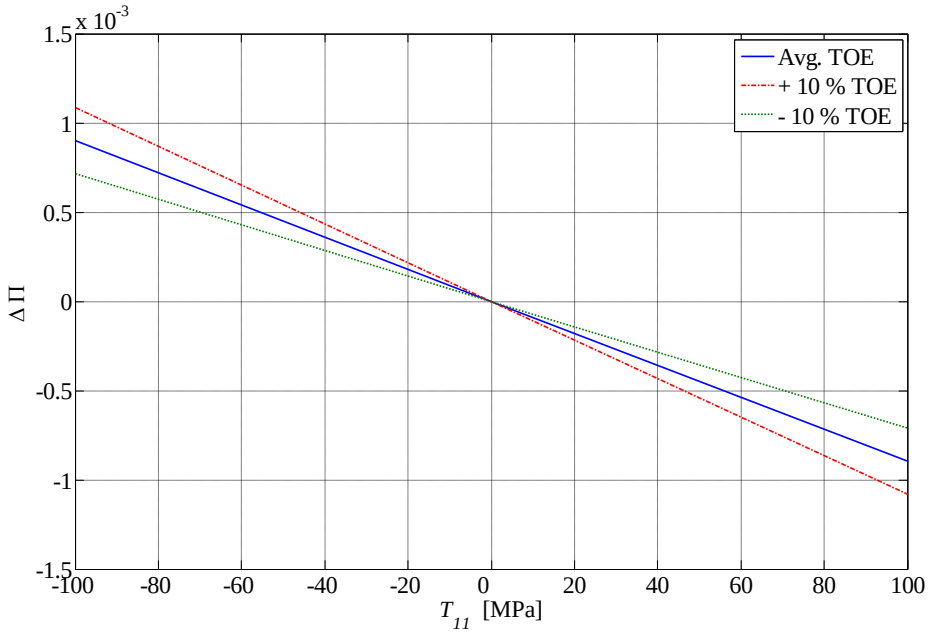

(b) Relative change in polarization.

Fig. 5.3. Effect of variation in TOE constants on relative change in Rayleigh wave speed and polarization.

5.3.3. Sensitivity of TOE Constants – Longitudinal and Shear Waves

In order to study the effect of variations in TOE constants for longitudinal and shear waves, a 10% scatter of the constants is assumed, as described in the previous section. Table 5.6 shows the variation in TOE constants used in the analysis.

Table 5.6. Variation of TOE constants-Bulk Waves [GPa]

	Min. (-10%)	Average	Max. (+10%)
l	-272.8	-248	-223.2
m	-685.3	-623	-560.7
n	-785.4	-714	-642.6

From Fig. 5.4 it is observed that the scatter in longitudinal wave speed is less as compared to the scatter in shear wave speed. This means that the variability in TOE constants has more effect on shear waves. Table 5.7 shows the influence of TOE constants on the sensitivity constants.

Table 5.7. Variation in sensitivity constants-Bulk Waves

	$(k_c)_L$	$\Delta(k_c)_L$	$(k_c)_S$	$\Delta(k_p)_S$
	[1/MPa]	%	[1/MPa]	%
Max.	-0.977E-05	-19.44	-1.324E-07	-89.10
Avg.	-1.214E-05	0.000	-1.220E-06	0.000
Min.	-1.450E-05	19.44	-2.308E-06	89.10

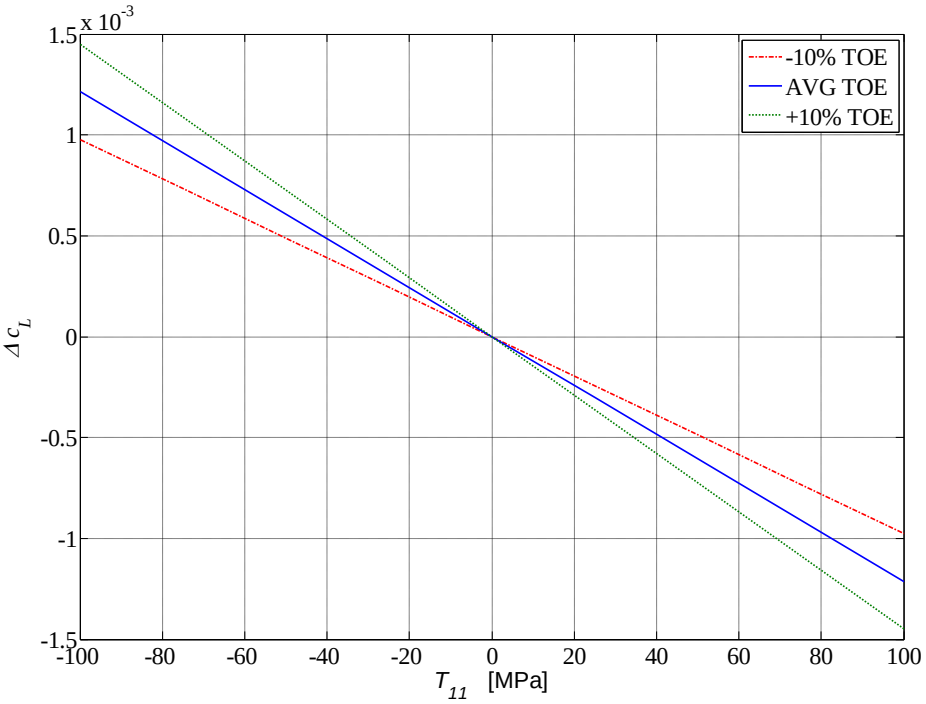

(a) Relative change in longitudinal wave speed.

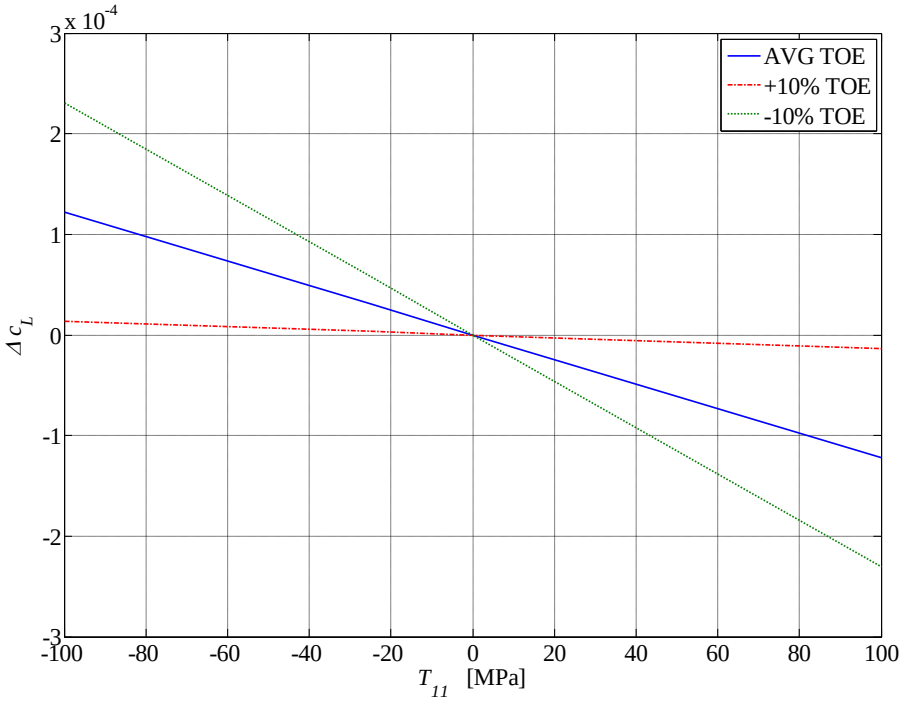

(b) Relative change in shear wave speed.

Fig. 5.4. Effect of variation in TOE constants on relative change in longitudinal wave speed and shear wave spe

5.3.4. Lamb Waves

Fig. 5.5 shows the dispersion curves for the symmetric and antisymmetric Lamb modes, shear wave and longitudinal wave for a frequency range of 0-10 MHz. This dispersion curve is plotted at zero stress. The numerical model is run for a stress variation between −400 MPa and +400 MPa. The dispersion relations obtained are used to determine phase velocity and group velocity in rail steel using Eq. (4.36) and Eq. (4.37). The Lamb wave velocities vary as a function of frequency and stress. Fig. 5.6 and 5.7 show the dispersion curves of the Lamb wave phase velocities and group velocities at zero stress. It is observed that at frequencies higher than about 6 MHz, the phase velocity in the S0 and A0 modes converges to the Rayleigh wave speed. The higher modes also tend to converge towards the S0 or A0 modes, at very high frequencies. Group velocities for all the modes increase steeply for a very small frequency change, reach a peak value, drop down to a lower level and finally converge towards the Rayleigh wave speed at higher frequencies.

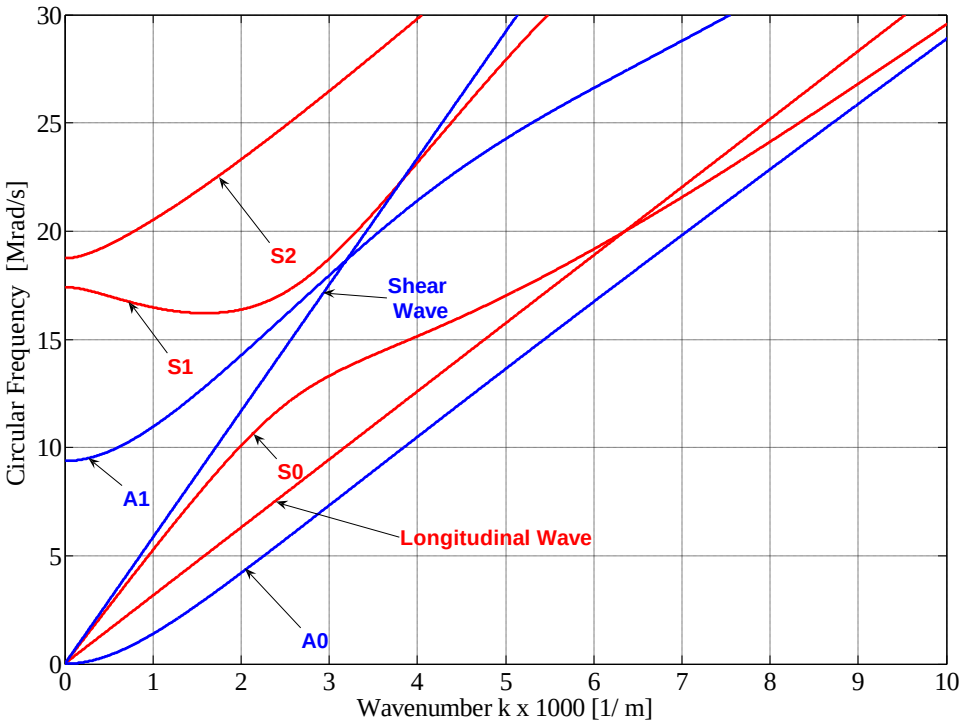

Fig. 5.5. Dispersion curves determined from the analytical model

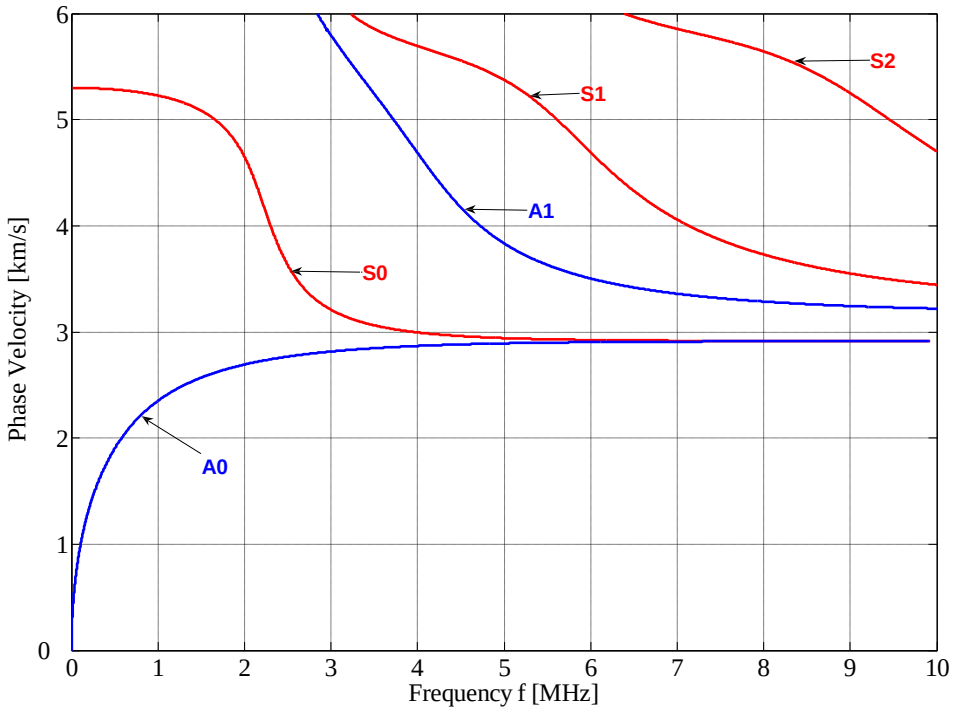

Fig. 5.6. Dispersion of Lamb modes phase velocity for zero stress

Fig. 5.8 and 5.9 show the change in phase velocity and change in group velocity with frequency for a stress change of 100 MPa. It is observed that, for Lamb waves the change in the phase and group velocity with stress varies with the frequency, since Lamb waves are dispersive. For Lamb waves the results predicted that at frequencies higher than 6 MHz the relative change in the wave speed is fairly constant. Hence, this value of the relative change is used to compare it with the sensitivities of other non-dispersive waves.

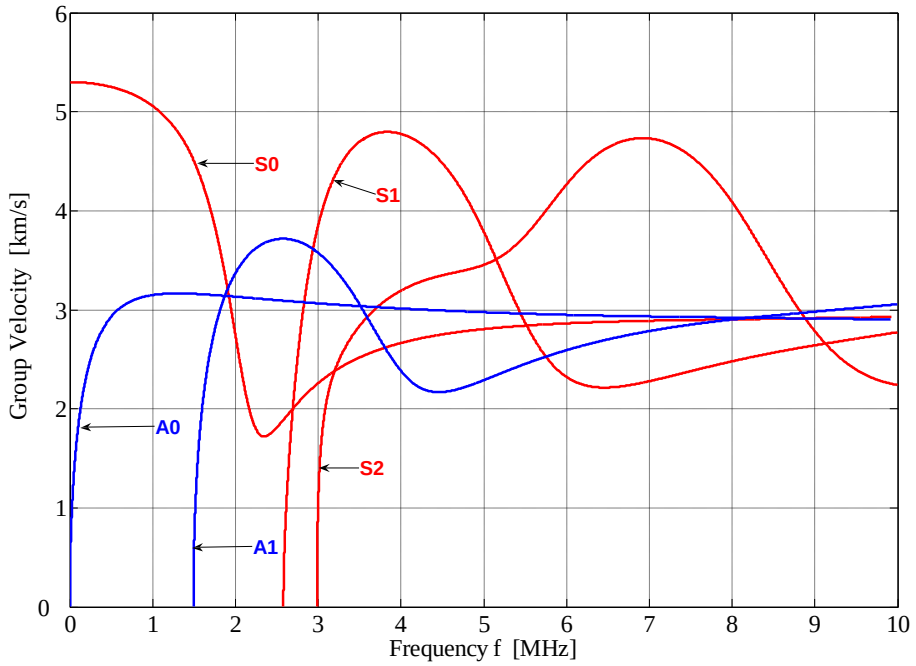

Fig. 5.7. Dispersion of Lamb modes group velocity for zero stress

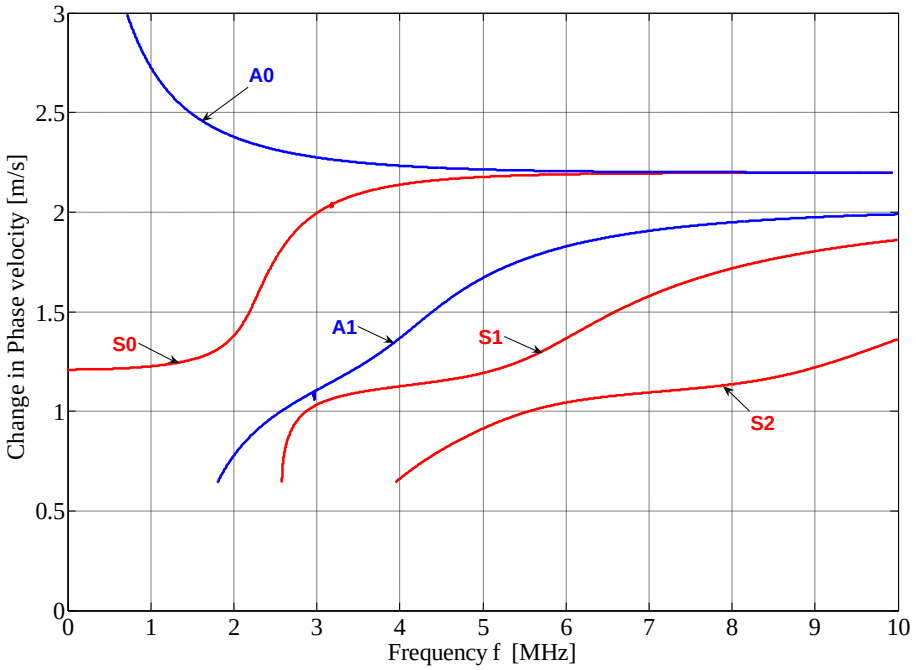

Fig. 5.8. Change in the phase velocity of Lamb modes for a stress change of 100 MPa

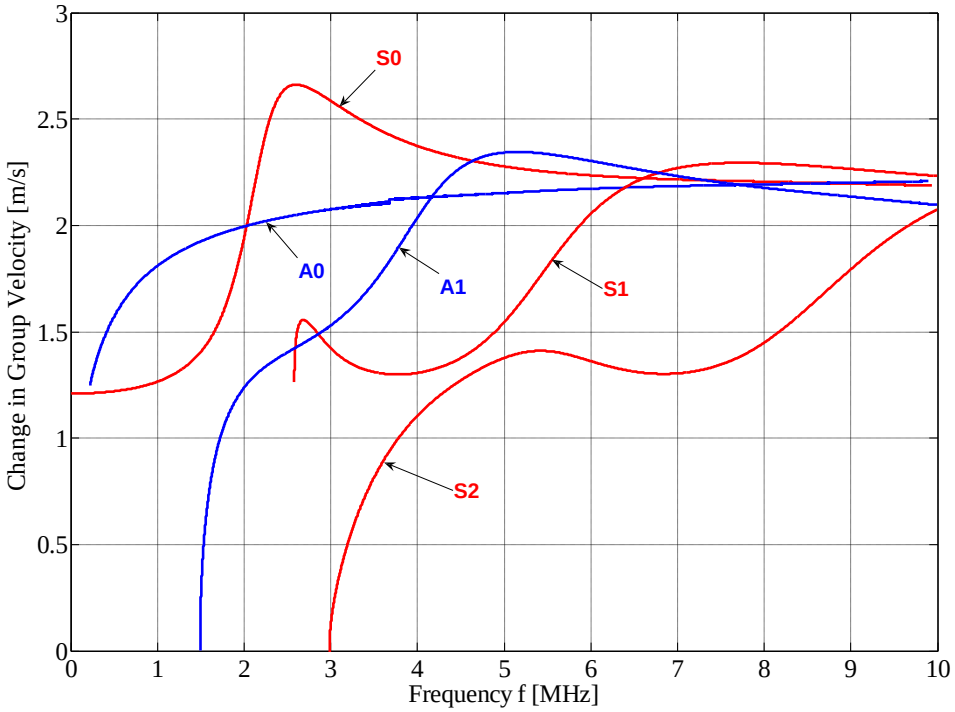

Fig. 5.9. Change in the group velocity of Lamb modes for a stress change of 100 MPa

5.3.5. Comparison of Sensitivity Constants

A comparison of the relative changes in wave speed and polarization is presented in Fig. 5.10. Table 5.8 presents a comparison of sensitivity constants for the various ultrasonic waves considered. It is observed that the Rayleigh wave speed has the maximum sensitivity and shear waves have the least.

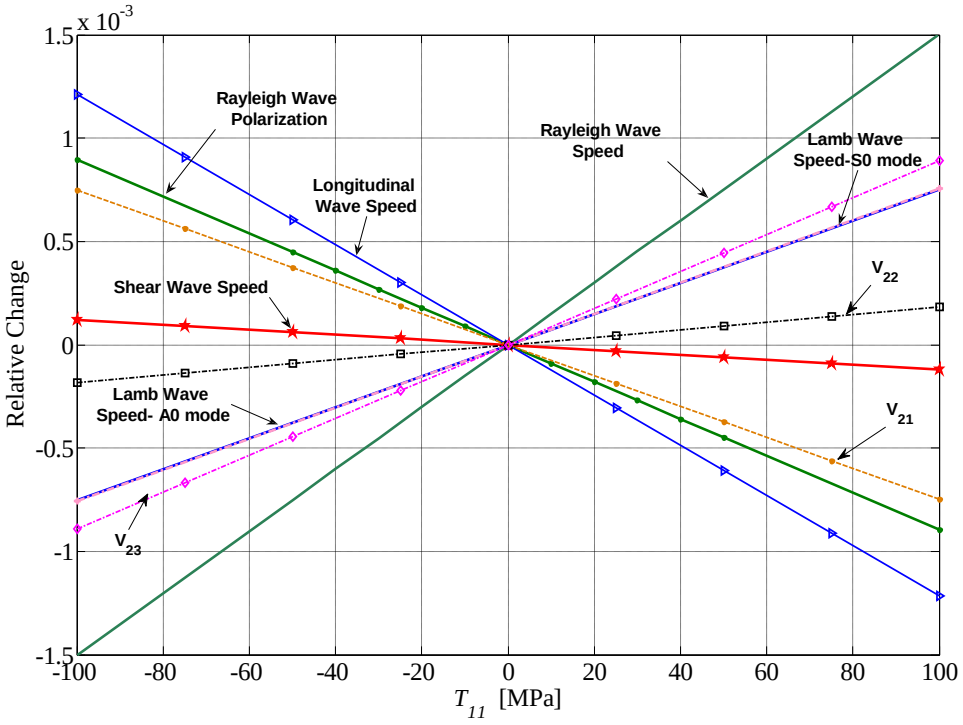

Fig. 5.10. Sensitivity of acoustoelastic effect

Table 5.8. Sensitivity constants for various ultrasonic waves

Type of Ultrasonic Wave	Rayleigh Wave		Lamb Wave	Longitudinal Wave	Shear Wave
Sensitivity Constants [1/GPa]	k_c	k_p	k_c	k_c	k_c
	15.03E-03	-9.011E-03	7.460E-03	-12.14-03	-1.22E-03

5.4. Conclusion

The numerical simulation results predict that the change in wave speed and polarization of ultrasonic waves as a function of the applied stress can be effectively used to measure the residual stresses in rails. Table 5.8 shows a comparison of the

sensitivity constants. It is seen that k_c for Rayleigh wave speed is the largest. In other words, the change in Rayleigh wave speed is most sensitive to the change in stress. The variations in TOE constants show a greater effect on wave polarization than on wave speed. A comparison of the Rayleigh wave sensitivity constants for rail steel with those of other materials described by Junge (2003) shows that the results are consistent with his observations that the stronger the material the smaller are the changes in wave speed and polarization. It is concluded that Rayleigh waves would be most feasible for determining the applied stresses in rail steel. All further study is carried out considering Rayleigh waves only.

CHAPTER VI

EXPERIMENTAL METHOD AND RESULTS

This chapter provides the details of the experimental procedure followed during the course of the research and presents the results obtained. The first section describes the principle followed for generating Rayleigh waves. The second section discusses the equipment/instrumentation involved and the third section describes the actual procedure engaged. Finally, the results of the experiments are discussed.

6.1. Principle of Wave Generation

The technique used in this research for generation of Rayleigh waves is referred to as wedge-technique. This technique has several advantages as put by Junge (2004). Firstly, this technique is frequency independent. Secondly, the technique theoretically generates only Rayleigh waves and hence interference from longitudinal and shear is not a problem. Thirdly, a sinusoidal longitudinal is converted to a sinusoidal surface wave. In this technique a longitudinal transducer is mounted on a plexiglass wedge and which in turn is coupled over the surface where the wave needs to be generated.

6.1.1. Mode Conversion

When ultrasonic energy is incident on a surface there is mode conversion of the incident energy at the interface. The incident energy is mode converted to different forms of ultrasonic energy in the second material and part of it is also reflected back. The mode conversion ultimately depends on the angle of incidence of wave energy as given by Snell's law. This is shown in Fig. 6.1.

In Fig. 6.1, an incident longitudinal wave is mode converted into a longitudinal, shear and Rayleigh wave in Material 2. Snell's law for each of this conversion can be expressed as

$$c_{\mathrm{L}}^{(1)} \sin\theta_{2\mathrm{R}} = c_{\mathrm{R}}^{(2)} \sin\theta_{1\mathrm{L}} \text{ ------ for Rayleigh wave,} \tag{6.1}$$

$$c_{\mathrm{L}}^{(1)} \sin\theta_{2\mathrm{L}} = c_{\mathrm{L}}^{(2)} \sin\theta_{1\mathrm{L}} \text{ ------ for longitudinal wave,} \tag{6.2}$$

$$c_{\mathrm{L}}^{(1)} \sin\theta_{2\mathrm{S}} = c_{\mathrm{S}}^{(2)} \sin\theta_{1\mathrm{L}} \text{ ------ for shear wave,} \tag{6.3}$$

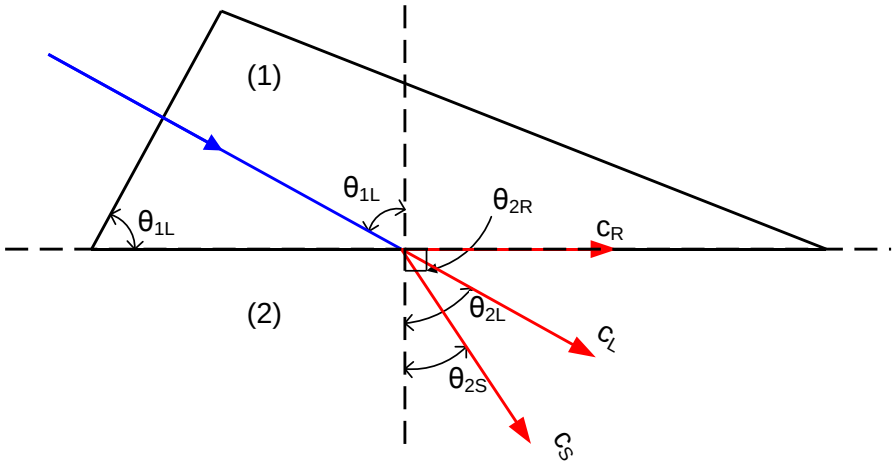

Fig. 6.1. Mode conversion

where R, L and S represent Rayleigh, longitudinal and shear wave respectively, and the numbers (1) and (2) represents the first and second material as shown in Fig. 6.1. For a surface wave, $\theta_{2\mathrm{R}} = 90°$, and Eq. (6.1) becomes,

$$\sin\theta_{1\mathrm{L}} = \frac{c_{\mathrm{L}}^{(1)}}{c_{\mathrm{R}}^{(2)}} = \sin\theta_{W} \ , \tag{6.4}$$

where *W* represents the wedge. Plugging in the above relationship in Equations (6.2) and (6.3),

$$\sin\theta_{2\mathrm{L}} = \frac{c_{\mathrm{L}}^{(2)}}{c_{\mathrm{R}}^{(2)}} \text{, and } \sin\theta_{2\mathrm{S}} = \frac{c_{\mathrm{S}}^{(2)}}{c_{\mathrm{R}}^{(2)}} . \tag{6.5}$$

For a material such as rail steel, it is known that, $c_{\mathrm{R}}^{(2)} < c_{\mathrm{S}}^{(2)} < c_{\mathrm{L}}^{(2)}$. Thus, Eq. (6.5) becomes greater than one and such solution does not exist. As a result, the mode

conversion yields a pure surface wave if the angle of incidence is θ_w as shown in Fig. 6.2.

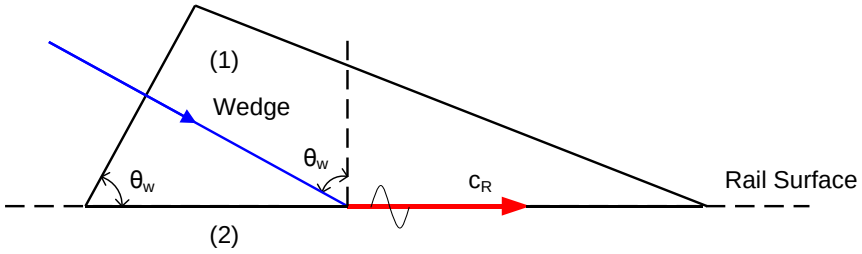

Fig. 6.2. Rayleigh wave generation

Thus, the wedge technique requires that the Rayleigh wave speed in the test material should be less than the longitudinal and shear wave speed in the wedge material, $\left(c_{\mathrm{R}}{}^{(2)} < c_{\mathrm{L}}{}^{(1)}, c_{\mathrm{R}}{}^{(2)} < c_{\mathrm{S}}{}^{(1)}\right)$. For rail steel the Rayleigh wave speed is 2966.67 m/s and the longitudinal wave speed through a plexiglass wedge is 2720 m/s. This gives an angle $\theta_w = 66.5^{\circ}$.

6.2. Experimental Setup

Fig. 6.3 shows a schematic diagram of the experimental setup. Following paragraphs shall discuss about the various components involved.

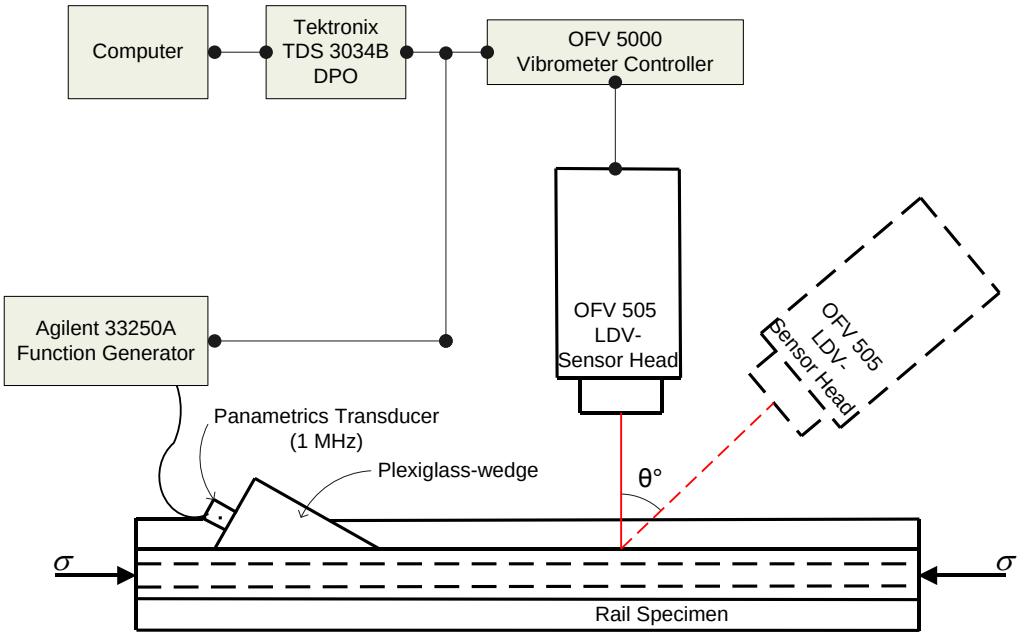

Fig. 6.3. Schematic diagram of the experimental setup

6.2.1. Laser Doppler Vibrometer (LDV)

The interferometer used in the experiments is a Polytec Single Point Vibrometer which comprises of OFV 505/503 standard sensor head and OFV 5000 vibrometer controller. This system measures the vibrations of a surface in the direction of the laser beam.

The basic principle of this system is to measure the frequency shift known as Doppler shift of the incident and reflected laser beam and relate it to the particle velocity and displacement. To detect this, laser from the interferometer is split into two beams, a reference beam and a measurement beam. The reference beam contains information about the original beam and is directly incident on a photodetector. The measurement beam is incident on the test specimen. The reflected beam changes in frequency and phase, due to surface vibrations. This back-scattered light contains information about the phase and frequency shift. This beam now falls on the photodetector and is compared with the reference beam which generates a modulated detector output signal revealing

the Doppler shift in frequency f_D and phase. The frequency modulation provides the velocity information and, the displacement information is revealed from the phase modulation.

(a) Out-of-plane measurement: In order to determine the out-of-plane velocity the laser and the test specimen are positioned orthogonal as seen in Fig. 6.4(a). This setup directly gives the out-of-plane particle velocity.

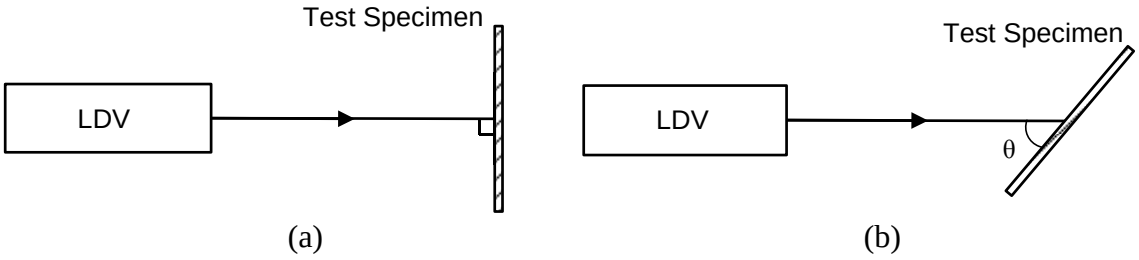

Fig. 6.4. In-plane and out-of-plane measurements

(b) In-plane measurement: In order to determine the in-plane velocity, the laser is incident at an angle θ with the test specimen as seen in Fig. 6.4(b). Under this setup the LDV measures velocity in the direction of the laser beam. Velocity measured in this manner contains the out-of-plane component which needs to be filtered out.

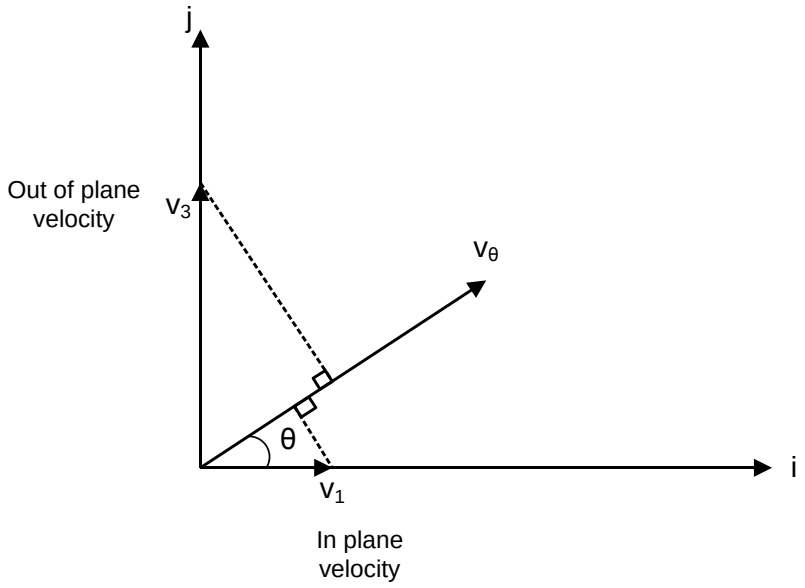

Fig. 6.5. Extracting in plane velocity

If v_θ is the velocity measured at an angle θ and v_3 is the out-of-plane velocity, then the in plane velocity v_1 is given by (Fig. 6.5)

$$v_1 = \left(v_\theta - v_3 \sin\theta\right) / \cos\theta \,. \tag{6.6}$$

For an angle of 45°,

$$v_1 = \left(v_\theta - \frac{v_3}{\sqrt{2}}\right)\sqrt{2} \,. \tag{6.7}$$

The LDV setup consists of a sensor head and a vibrometer controller (Fig. 6.6).

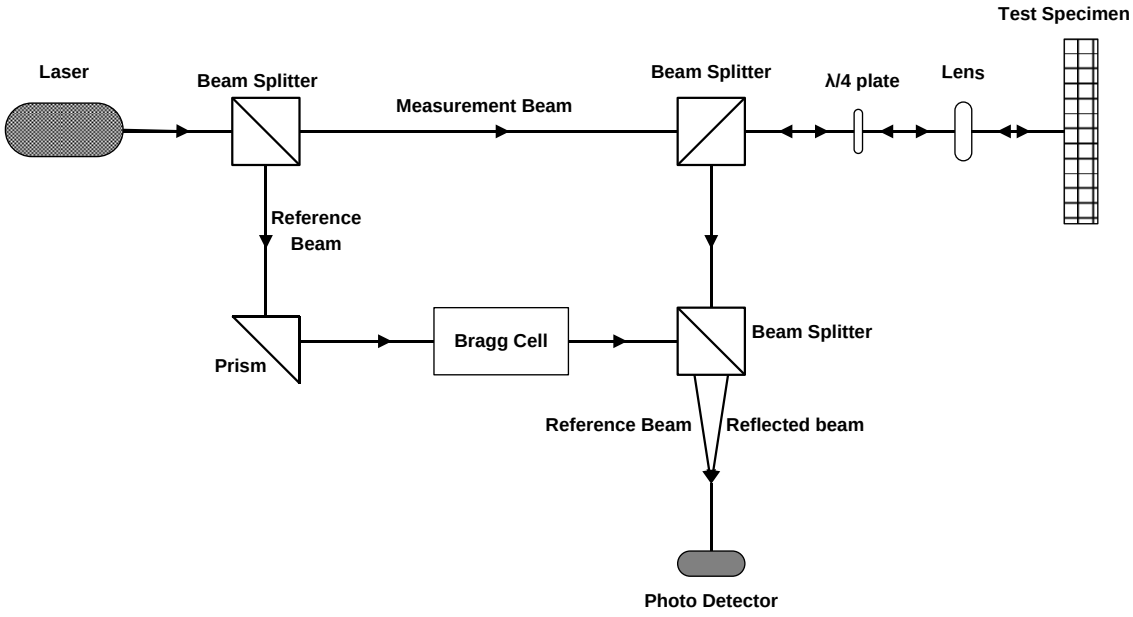

Fig. 6.6. Optical configuration in the LDV sensor head
(Polytec User Manual for OFV-505/-503 Sensor head)

The laser source is a Helium-Neon laser that generates a coherent polarized laser beam. The first beam splitter (BS-1) splits the beam into a measurement beam and a reference beam. The measurement beam passes through another beam splitter (BS-2) and a $\lambda/4$ plate and is incident on the test specimen. The reference beam passes through a Bragg cell and a third beam splitter (BS-3) before it is made incident on the photodetector. The reflected beam is deflected by BS-2 towards the photodetector where it mixes with the reference beam. The path of the reference beam from BS-1 to the photodetector is equal to the path of the measurement beam from BS-1 to photodetector through BS-2 and BS-3. Thus, the path difference between the reference and reflected beam is equal to twice the distance between BS-2 and the test specimen. The Bragg cell performs the function of determining the sign of the velocity. The mixed beam is converted to an electrical signal in the photodetector and analyzed in the controller.

The output passes through a built-in low pass filter of 1.5 MHz and a fast tracking filter. The output is displayed in terms of $mm/s/V$.

6.2.2. Input Signal

The transducer is driven by a sinusoidal signal or an impulse. The sine function is generated using an Agilent 33250A function generator capable of generating frequencies up to 80 MHz. The pulse is generated using Panametrics Pulser/ Receiver PR 5072.

6.2.3. Transducer

The experiment uses a Panametrics C401 transducer for wave generation. The transducer has a size of $0.5" \times 1"$ and a center frequency of 1 MHz.

6.2.4. Data Acquisition

The signal from the vibrometer controller is passed on to a digital phosphor oscilloscope (DPO). The DPO is a Tektronix TDS 3034B. The signal is averaged over 512 times by the oscilloscope. The waveform is acquired on a computer using *Wavestar* software. The data is analyzed using MATLAB.

6.2.5. Test Sample

The test sample is a $12"$ long rail piece with bottom flange dimensions $6" \times 12"$ and $7"$ deep with a cross section of 12.88 in^2.

6.3. Experimental Procedure

6.3.1. Surface Preparation

As described in Section 6.2.1, the principle of laser vibrometry is based on comparing and analyzing the reference and the reflected beams. Thus it is essential that the surface reflects back most of the energy incident on it. A highly reflective surface such as a mirror reflects ideally all the energy when light is incident orthogonal to the surface. However, when the light is incident at another angle that is not orthogonal, the light is reflected away from the lens. The OFV-505 sensor head has a collecting aperture of 10 mm diameter. Any energy reflected outside this diameter is not useful for analysis.

Diffuse surfaces reflect light over a large area and dull surfaces absorb most of the incident light.

In order to obtain good results it is necessary to increase the reflectivity of the surface by using external agents such as retro-reflective tape or paints. Tapes are not effective since the thickness of the tape may generate Lamb waves within the tape. Retro-reflective paints contain glass beads or spheres mixed with a base and are available in the form of liquid paints or aerosols. When a coherent beam is incident on such a material, a speckle pattern is generated due to multiple reflections from the small glass beads. The laser beam hits a large number of glass beads simultaneously and this results into interference effects between the beams originating at different scattering centers on the surface. If the focused spot is very small, the number of scattering centers is small and the angular dependence of the path length differences in a given direction is also small. This leads to a large angle over which the interference condition is reasonably constant and thus a large solid angle for the speckle. The test specimen used in this research is coated with *"RUSTOLEUM Reflective Finish"* which is an aerosol and works on a similar principle as explained above.

6.3.2. Velocity and Polarization Measurement

The experimental setup is shown in Fig. 6.3. The plexiglass wedge is clamped in position on the rail web. The transducer is mounted on the wedge such that the wave is incident at the critical angle as determined in Section 6.1.1. DOW CORNING high vacuum grease is used as a coupling agent between the transducer and wedge and between the wedge and test specimen to lower the acoustic impedance between two surfaces.

The transducer is driven by a sinusoidal signal with maximum peak to peak amplitude of 10 Volts and a frequency of 1 MHz. The number of cycles is varied between 1 and 10. Alternately, the transducer can be driven by a single pulse with

amplitude varying between 90 V and 380 V. To obtain the in-plane and out-of-plane components at a point on the specimen, it is necessary to take two measurements. It is advisable to keep the laser running for at least 30 minutes before the measurements are made to heat up and give a stable light. The laser is focused into a small spot on the surface and two measurements are taken as described in Section 6.2.1. The specimen is stressed in a compression testing machine and the experiment is repeated. Fig. 6.7 shows the experimental setup with the rail specimen mounted on a testing machine and two LDV's focused on the surface. Fig. 6.8 shows a picture of the rail sample fixed in the testing machine. The change in the Rayleigh wave components is observed and compared to the analytical results.

Fig. 6.7. Experimental setup for Rayleigh wave measurement

Fig. 6.8. Rail specimen mounted on a compression testing machine

6.4. Results

To begin with, the experiment is carried out with the specimen in the unstressed case. Several measurement techniques for determining the Rayleigh wave polarization are investigated and results compared. Subsequently, the specimen is stressed, and the experiment repeated.

6.4.1. Unstressed Case

6.4.1.1. Excitation Signal

Experimental data was obtained for two types of excitation signals and results examined.

(a) Sinusoidal Signal

The transducer is excited with a 10 cycle sinusoidal signal. The amplitude of the signal is set to 10 Volts peak to peak. To achieve optimum signal quality, the signal frequency is set equal to 1 MHz which is also the transducer frequency. The signal repetition rate is set to 50 ms, ensuring that the first set of 10 cycles dissipate completely before the arrival of the next set. The received signal is averaged over 512 times.

The Rayleigh wave velocity is measured at a distance of 60 mm from the point of generation. The vibrometer output for out-of-plane measurement is shown in Fig. 6.9. It is observed that the Rayleigh wave arrives at 33 μs which is in good agreement with the theoretically expected arrival time of 32.36 μs.

It is observed from Fig. 6.9 that the peaks of the vibrometer output signal are not steady. As explained in Section 6.1.1, when a disturbance is incident at the critical angle, only Rayleigh waves are generated. However, the observed instability of amplitudes might be explained by the possible interference of longitudinal and shear waves. The expected arrival times for a distance of 60 mm are estimated in Table 6.1. Thus, for a 10-cycle sinusoidal wave with a period of 1 μs, the longitudinal and shear waves do not dissipate completely before the arrival of Rayleigh wave. The discrepancy in theory and experimental observation may be attributed to the inaccuracy in setting the critical angle.

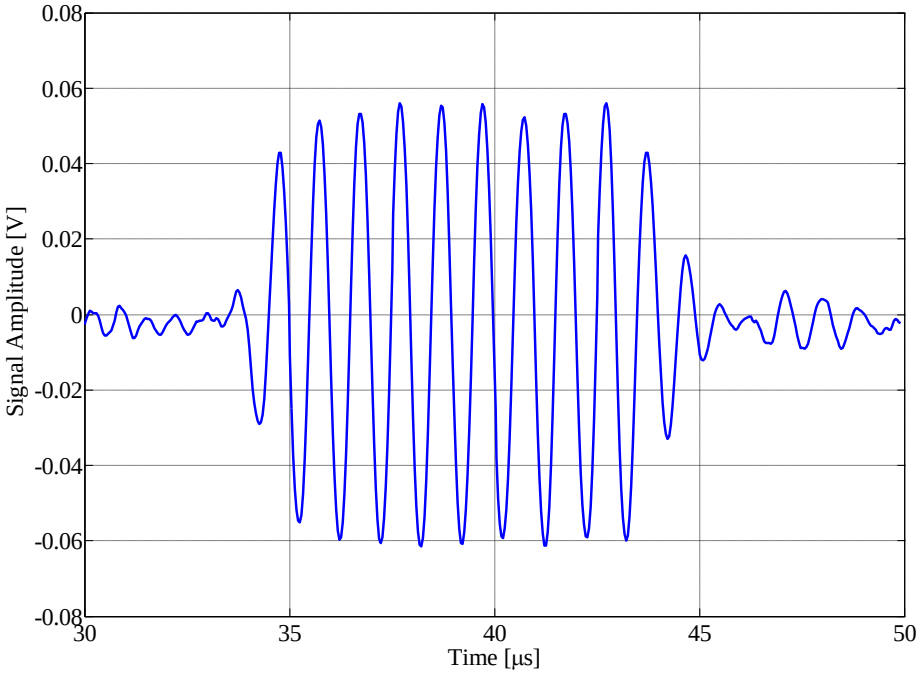

Fig. 6.9. Rayleigh wave out-of-plane component in unstressed specimen for sinusoidal input signal.

Table 6.1. Estimated arrival times of ultrasonic waves at a distance of 60 mm from the transducer

	Wave Velocity [m/s]	Estimated arrival time [μs]
Longitudinal Wave	5944.21	22.22
Shear Wave	3200.56	30.88
Rayleigh Wave	2966.67	32.36

(b) Impulse

In this case the transducer is driven by a single pulse of 380 Volts. The damping value is set to 500 ohms. The received signal is averaged over 512 times. Rayleigh wave velocity is measured at a distance of 60 mm from the point of generation. The vibrometer output for out-of-plane measurement is shown in Fig. 6.10.

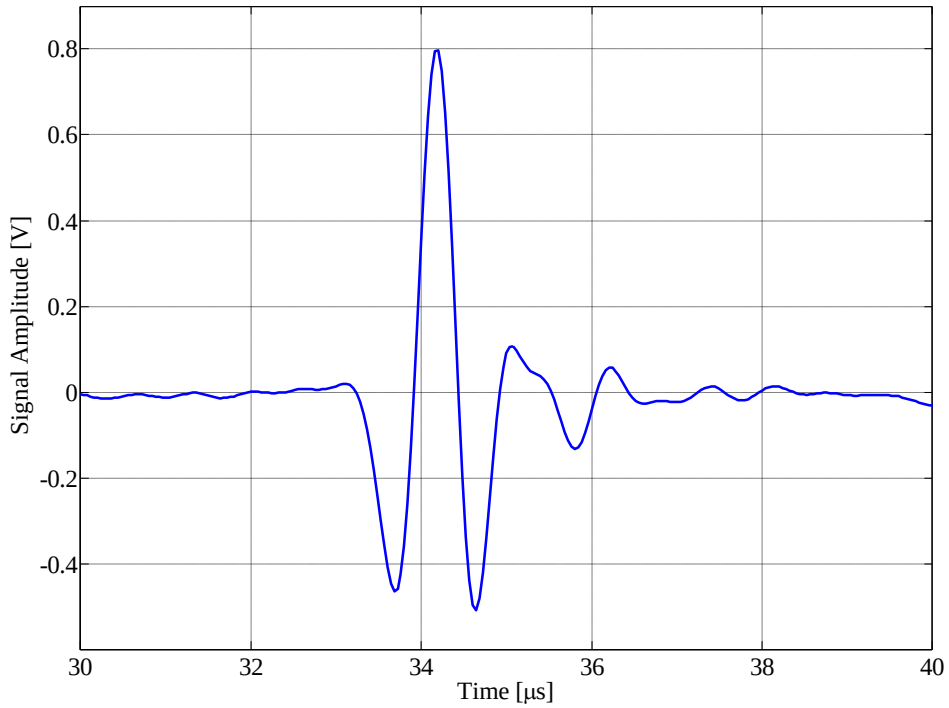

Fig. 6.10. Rayleigh wave out-of-plane component in unstressed specimen for pulse excitation

It is seen from Fig. 6.10 that the arrival time of 32.8 μs is fairly consistent with the estimated arrival time of 32.36 μs. Also, since the voltage applied was much higher, the signal to noise ratio (SNR) is higher.

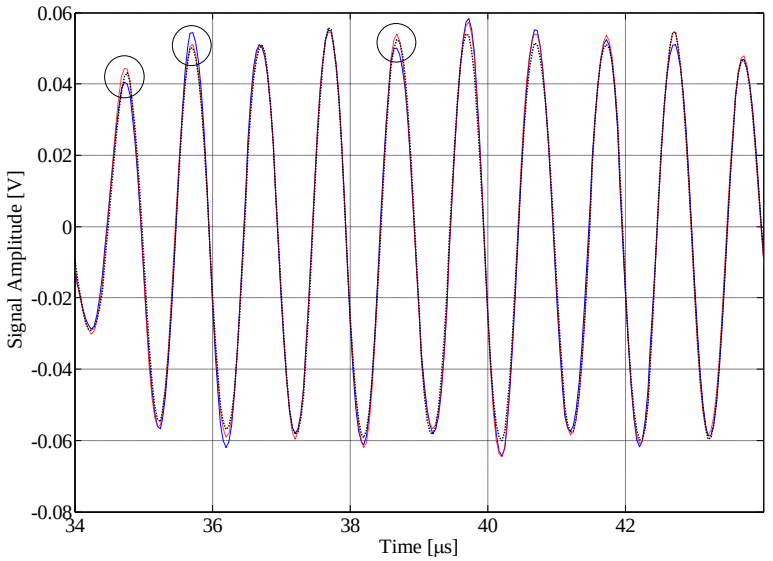

(a)

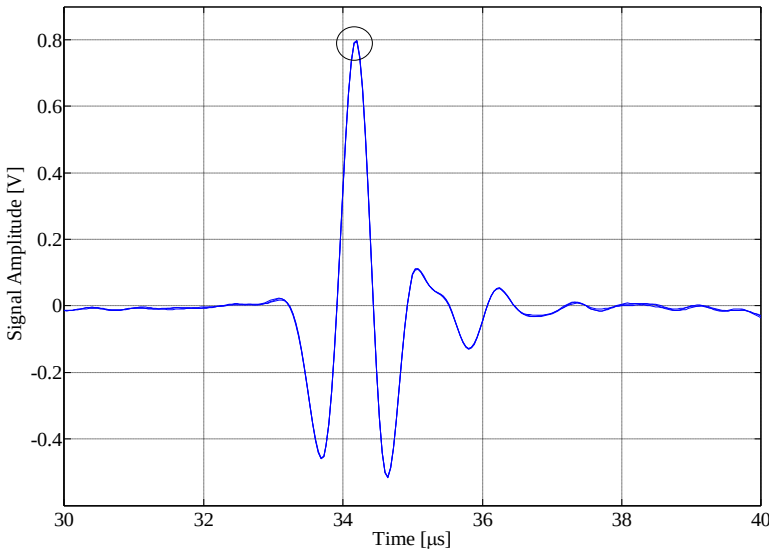

(b)

Fig. 6.11. Rayleigh waves in rail steel. (a) Excitation is 10 cycle sinusoidal signal. (b) Excitation is a pulse

A set of consecutive measurements were taken for both, sinusoidal signal excitation and pulse excitation. Rayleigh waves detected for each excitation are shown in Fig. 6.11. Comparing Figures 6.11 (a) and (b) reveal that the maximum peak amplitudes in Fig. 6.11 (a) have a much larger deviation than in Fig. 6.11 (b). This can be attributed to the interference explained earlier. In other words, the peaks in Fig. 6.11 (b) are fairly stable. In this case, there is negligible interference due to longitudinal or shear waves since the driving signal is a single pulse.

Conclusion

To avoid any interference issues, all further measurements are taken using the pulse as excitation.

6.4.1.2. Measurement Techniques

As explained in Section 6.3, the basic principle for measuring polarization is to take two measurements using LDV and separate the in-plane and out-of-plane components. The following techniques were investigated to determine polarization, keeping this principle in mind.

(a) Using Single Laser Doppler Vibrometer

The first technique utilizes a single LDV to make two measurements. This is shown in Fig. 6.11.

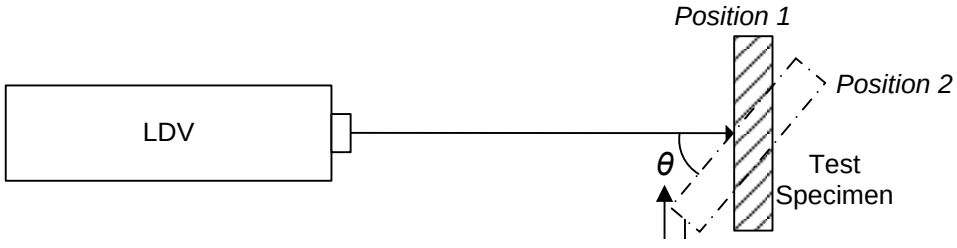

Fig. 6.12. Measurement using a single LDV

When the test sample is in position 1, the LDV measures the out-of-plane component of Rayleigh wave velocity. Under position 2, the LDV measures the component in direction θ. The in-plane component can be extracted using Eq. (6.6).

Results and Discussion

Fig. 6.13 presents the in-plane and out-of-plane components obtained using this technique. The polarization of Rayleigh wave is presented in Fig. 6.14. As can be seen, the polarization ellipse is rotated from the vertical axis. This indicates that the in-plane and out-of-plane components have a phase-shift not equal to $\pi/2$. Ideally, when the two components have a phase-shift of $\pi/2$, the ellipse has a perfectly vertical axis. This discrepancy can be explained due to the relative movement of the measurement point on the rail surface between position 1 and position 2 as shown in Fig 6.12. The erroneous rotation of the specimen from position 1 to position 2 results into the LDV detecting the wave at two separate points. This results into a phase shift in the two signals. This setup yields a mean polarization value of 0.6498 with a standard deviation of 0.01. It can be concluded that the results are not reproducible.

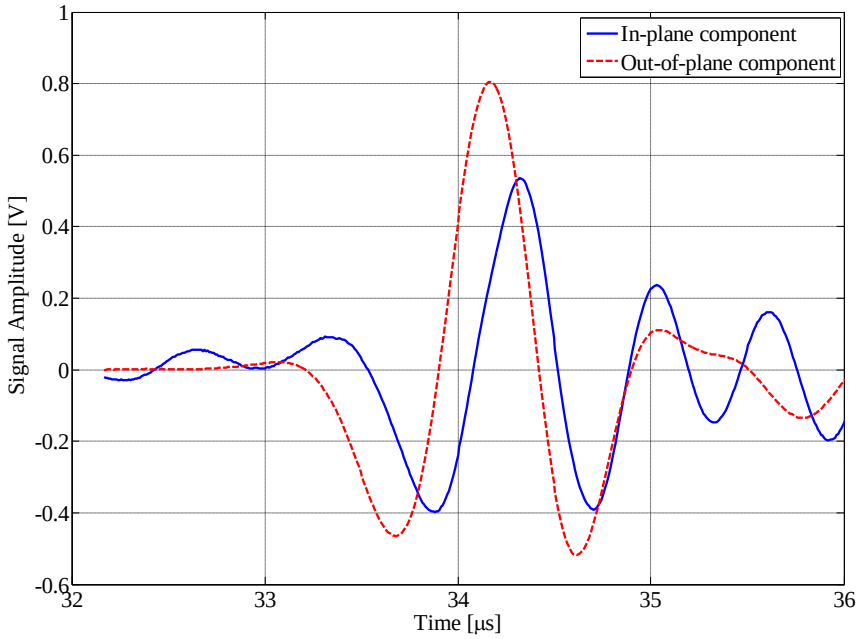

Fig. 6.13. Rayleigh wave components in unstressed specimen using single LDV

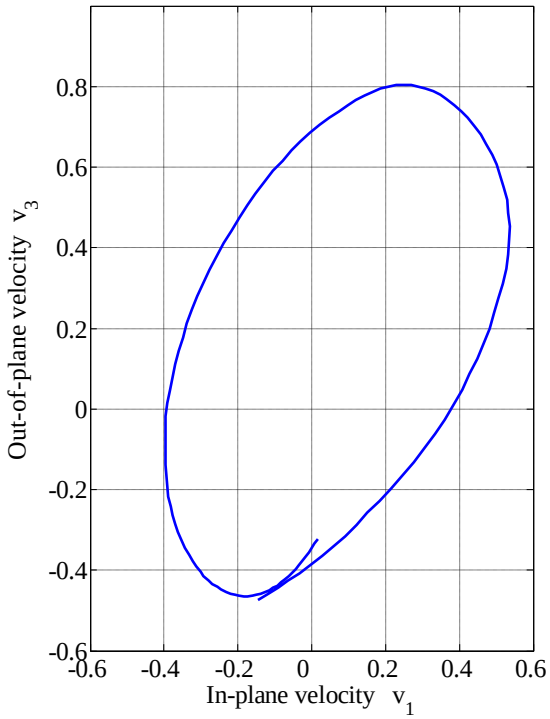

Fig. 6.14. Rayleigh wave polarization in unstressed specimen using single LDV

(b) Using Single Laser Doppler Vibrometer with a Combination of Beam Splitter and Mirror

As an alternative over the measurement technique described earlier, a single LDV was set up in combination with a beam splitter and mirror (Fig. 6.15).

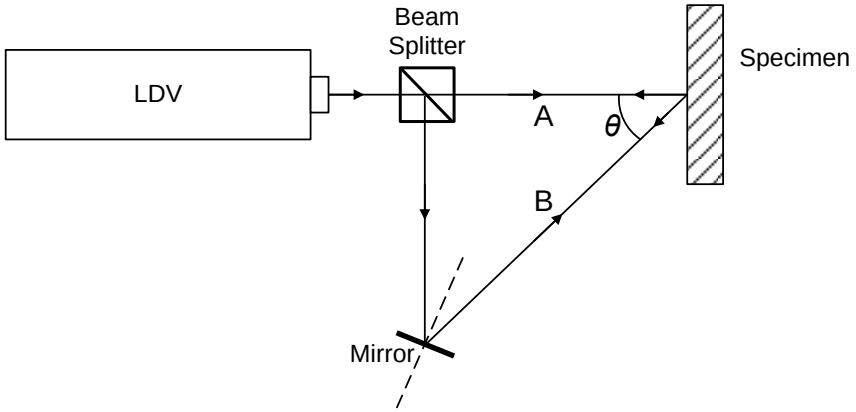

Fig. 6.15. Measurement using a single LDV and a beam splitter-mirror combination

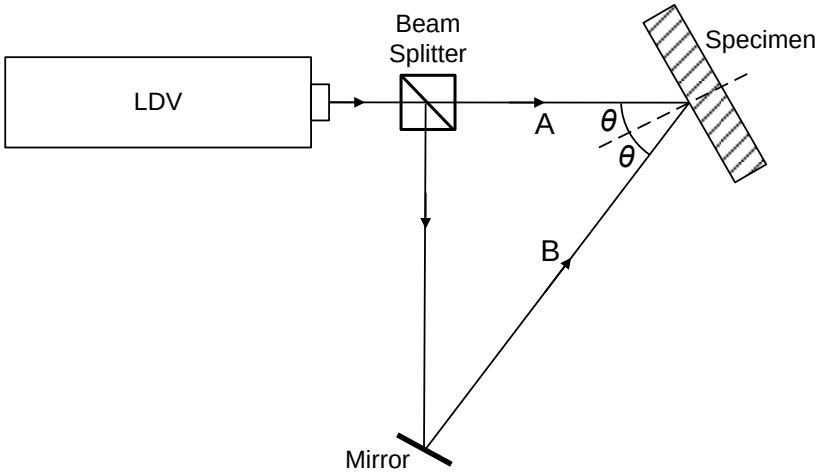

Fig. 6.16. Measurement using a single LDV and a beam splitter-mirror combination

In this setup, the drawback due to physical movement of the specimen is eliminated by using a combination of beam splitter and mirror. It facilitates measuring in-plane and out-of-plane components simultaneously. Two setups were investigated. In the first setup (Fig. 6.15), beam B is blocked to measure the out-of-plane component. To measure the in-plane component beam A is blocked and the in-plane component is obtained using Eq. (6.6). Fig. 6.18 shows the in-plane and out-of-plane velocity components obtained using this technique. Fig. 6.19 shows the polarization of the Rayleigh wave.

In the second setup (Fig. 6.16); two measurements are taken at an angle θ from the perpendicular to the rail surface. The in-plane and out-of-plane velocities can be obtained by

$$v_1 = \frac{(v_\theta)_A - (v_\theta)_B}{2} \quad , \tag{6.1}$$

$$v_3 = \frac{(v_\theta)_A + (v_\theta)_B}{2} \quad , \tag{6.2}$$

where $(v_\theta)_A$ and $(v_\theta)_B$ are the velocity components in direction of beam A and B, respectively and are shown in Fig. 6.17

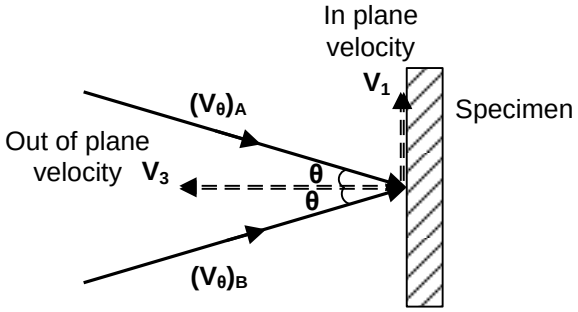

Fig. 6.17. Extracting in-plane and out-of-plane velocities using setup in Fig. 6.15

Results and Discussion

Both the setups were studied and no significant differences were observed in the results. The results for the setup in Fig. 6.15 are presented in Figures 6.18 and 6.19. It can be noted from Fig. 6.18 that the peak of in-plane component coincides with the zero value of out-of-plane component and vice-versa. This indicates that the two waves have a phase shift of $\pi/2$. As expected, the polarization ellipse is perfectly vertical (Fig. 6.19 (a)). A mean polarization value of 0.4506 with a standard deviation of 0.0085 was obtained with this setup.

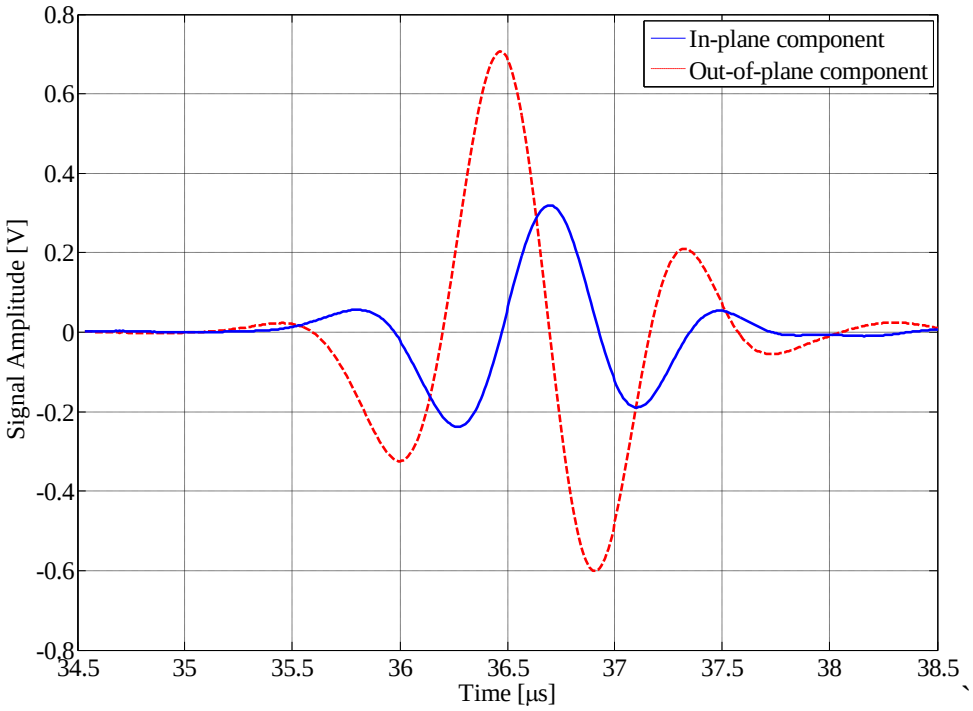

Fig. 6.18. Rayleigh wave components in unstressed specimen using single LDV and beam splitter - mirror combination with setup shown in Fig. 6.16

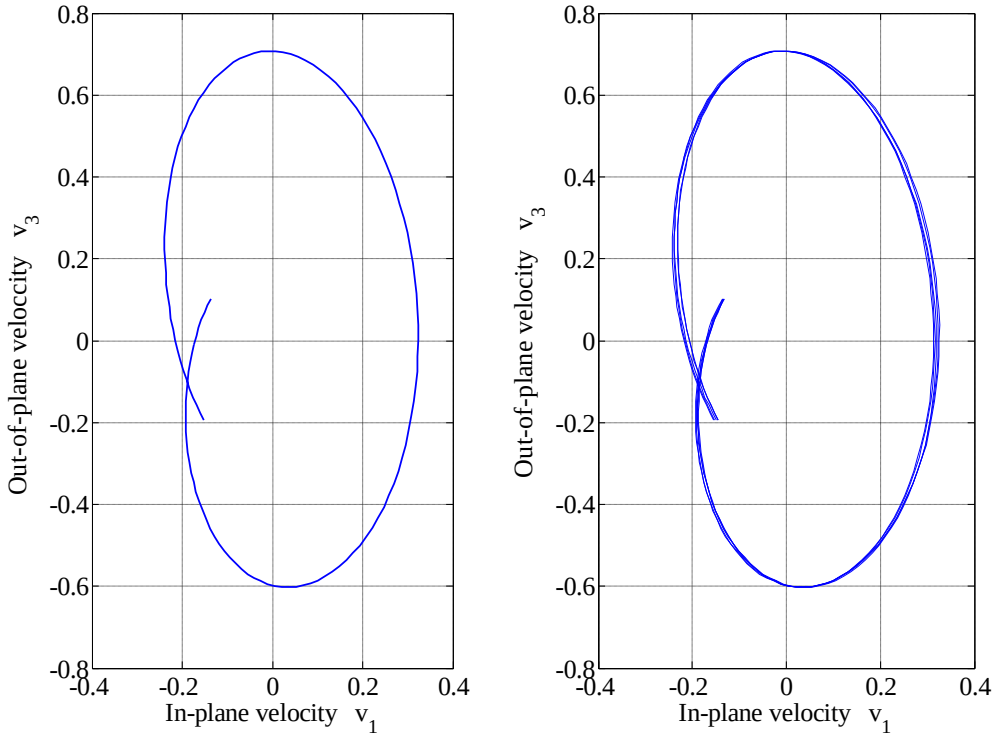

(a) **(b)**

Fig. 6.19. Rayleigh wave polarization in unstressed specimen using single LDV and beam splitter - mirror combination with setup shown in Fig. 6.16

Figures 6.20 and 6.21 present the velocity components and polarization, respectively, using the setup in Fig. 6.16. This setup gave a mean polarization of 0.4533 with a standard deviation of 0.007.

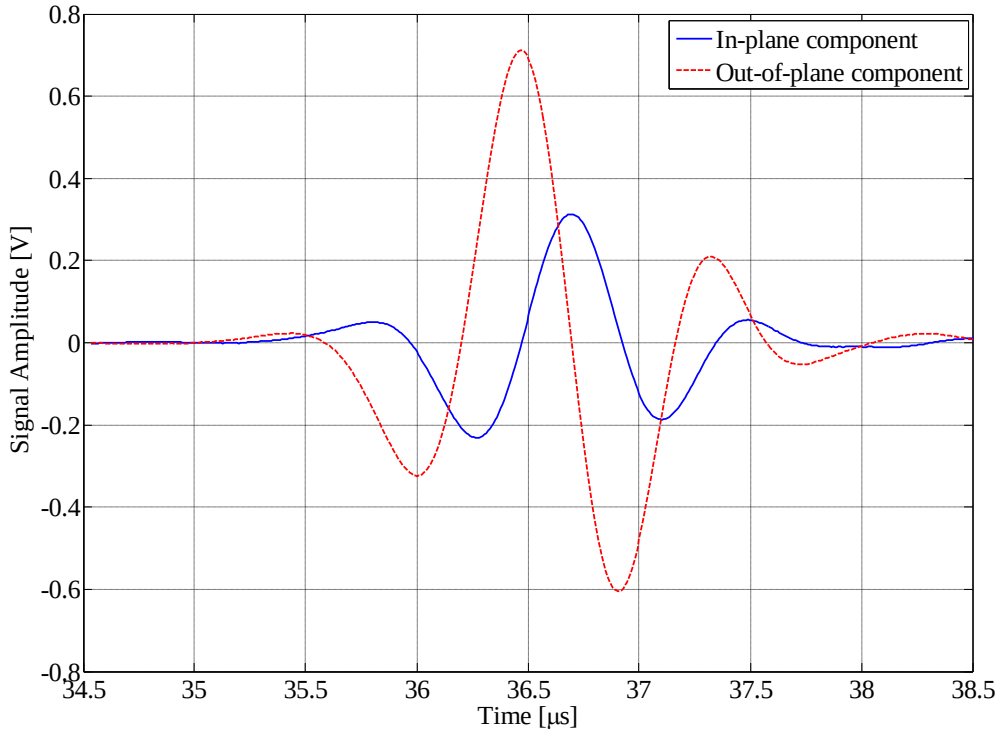

Fig. 6.20. Rayleigh wave components in unstressed specimen using single LDV and beam splitter - mirror combination with setup shown in Fig. 6.17

Again, the accuracy in measurement depends on how closely the two beams coincide. This setup encountered the problem of loss in laser energy as the beam splitter divided the beam into two. The effect of this is loss of carrier signal. Consequently, the maximum in-plane and out-of-plane components showed a considerable deviation. This deviation is observed in Figures 6.19 (b) and 6.21 (b).

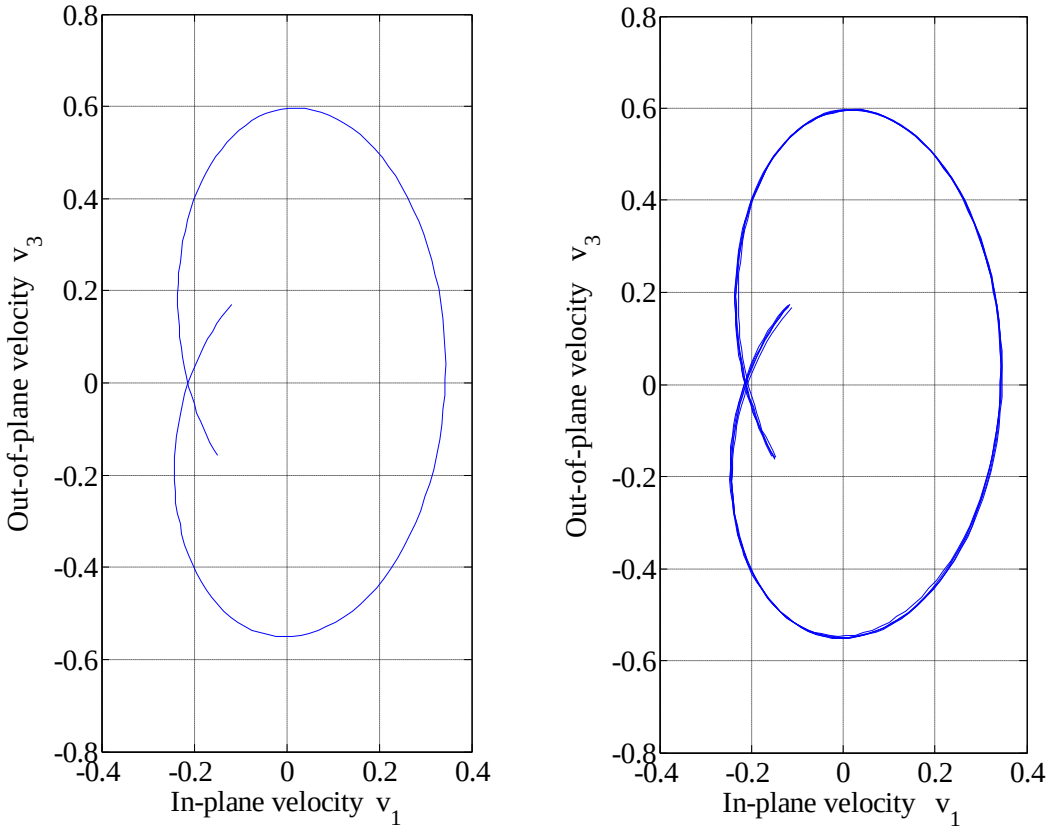

Fig. 6.21. Rayleigh wave polarization in unstressed specimen using single LDV and beam splitter - mirror combination with setup shown in Fig. 6.15

(c) Using two Laser Doppler Vibrometers

This setup utilizes two LDV's focused simultaneously at a single point on the specimen (Fig. 6.22). Beam A and Beam B measure components in the corresponding directions. The in-plane and out-of-plane components can be obtained using Equations (6.1) and (6.2).

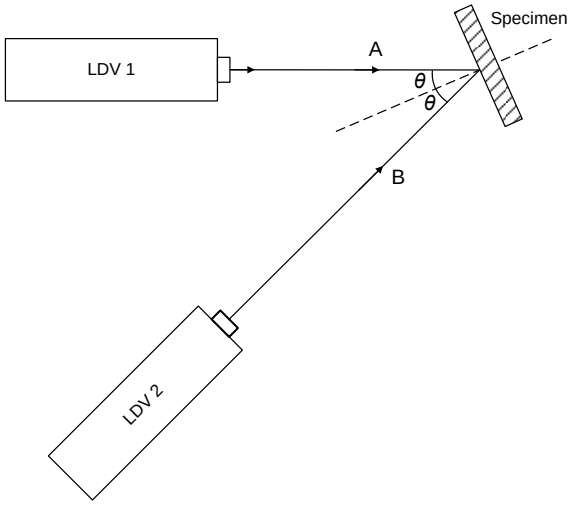

Fig. 6.22. Measurement using two laser Doppler vibrometers

Results and Discussion

This setup yielded the best results as compared to other methods investigated. The in-plane and out-of-plane components are shown in Fig. 6.23.

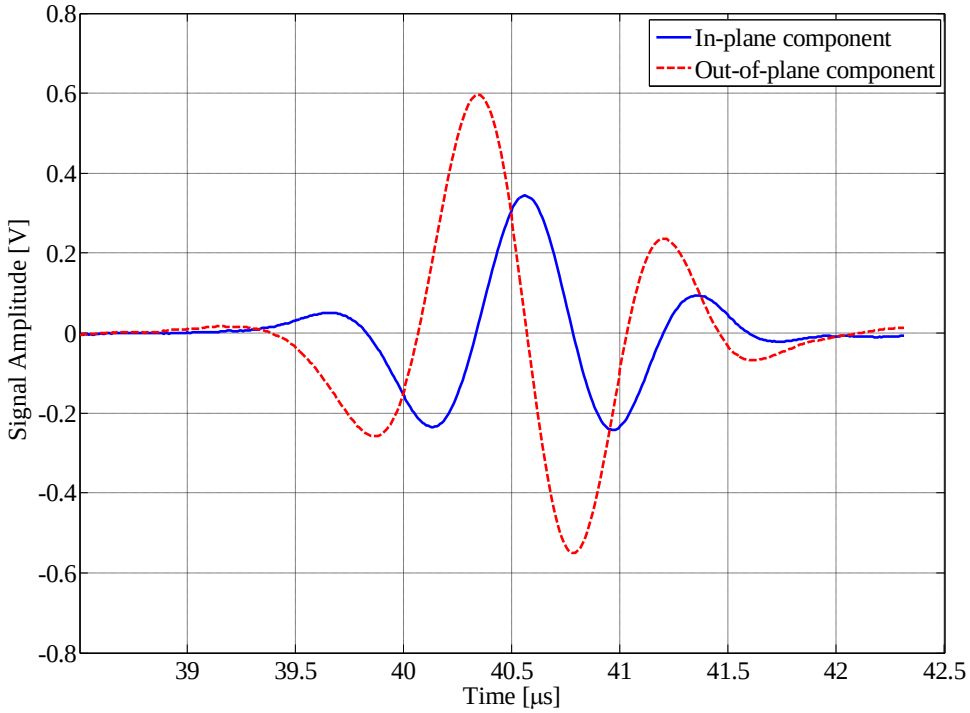

Fig. 6.23. Rayleigh wave components in unstressed specimen using two LDVs

Using two LDVs eliminates all problems encountered in earlier setups. As can be seen in Fig. 6.23, the in-plane and out-of-plane components are out of phase by $\pi/2$. The polarization ellipse is presented in Fig. 6.24. It is found that when measurements are repeated, the deviation in the maximum in-plane and out-of-plane components is less than the deviation observed in earlier setups. Once again, it is crucial to have the two laser beams focused at a single point. A mean polarization value of 0.5792 with a standard deviation of 0.0028 was obtained with this setup.

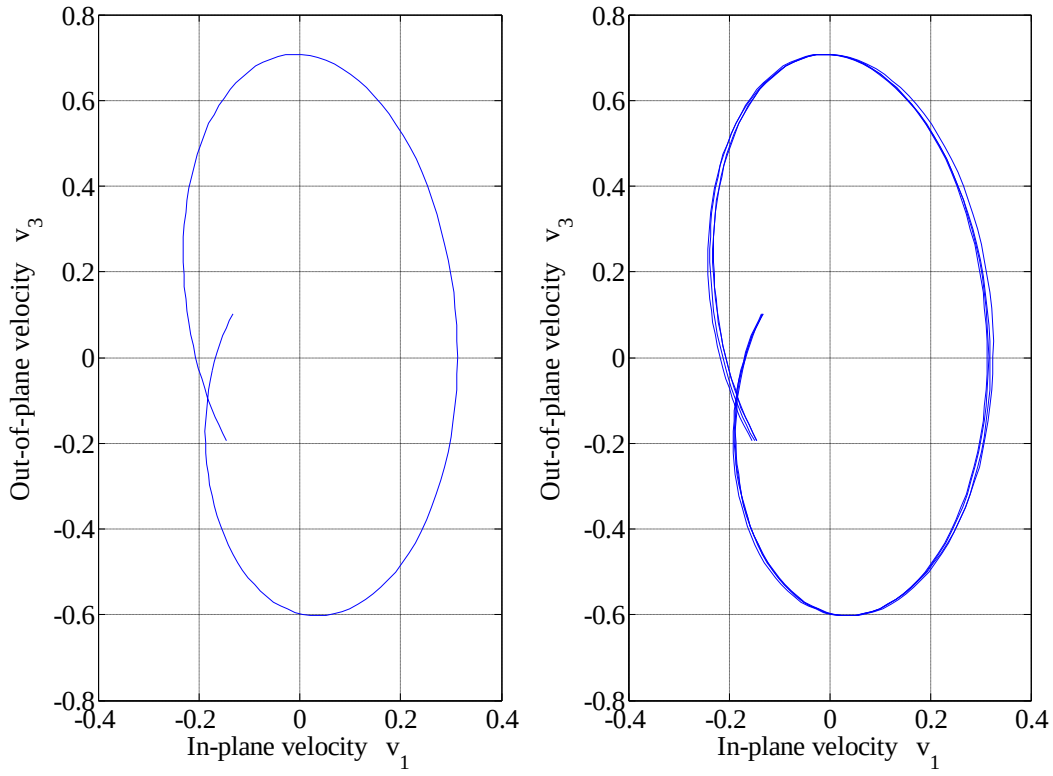

Fig. 6.24. Rayleigh wave polarization in unstressed specimen using two LDVs

Conclusion

Due to the comparative robustness of measurements obtained using two LDVs, further experiments are carried out using this setup.

6.4.2. Stressed Case

6.4.2.1. Measurement Description

The setup described in Fig. 6.22 is used to make the measurements. The transducer is driven by a pulser generating a pulse of 380 V. The specimen is compressed in a compression testing machine. The specimen is preloaded to generate a compressive stress of $T_{11} = -5.36$ MPa. Further, the specimen is loaded to generate a

compressive stress of $T_{11} = -214.15$ MPa. Rayleigh wave polarization is measured at a distance of 57 mm from the wedge.

6.4.2.2. Results

(a) Stress of 5.36 MPa

The signal shows a Rayleigh wave velocity of 2964.5 m/s which is in good agreement with the theoretical value of 2966.67 m/s. Fig. 6.25 shows the in-plane and out-of-plane velocity signals for the preloaded case. It is observed that the two components have a phase shift of $\pi/2$. The particle displacement components can be obtained by integrating the velocity signals. The polarization ellipse using velocity components and using displacement components are shown in Figures 6.27 (a) and (b), respectively. The maximum out-of-plane component is almost twice as high as the in-plane component. Polarization for this case can be obtained by

$$\Pi_{10} = \frac{u_1}{u_3} = \frac{v_1}{v_3}.$$

The velocity components give a mean polarization value of 0.49, while the displacement components yield a polarization value of 0.41. The numerical simulation gives a polarization value of 0.65. The standard deviation of measurements is 0.0046.

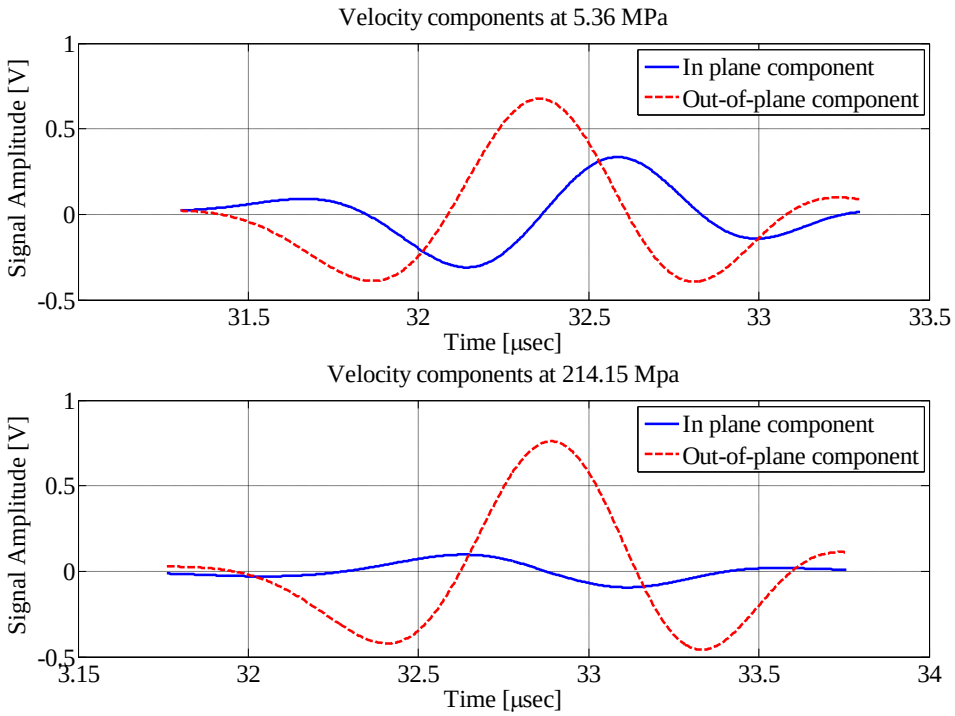

Fig. 6.25. In-plane and out-of-plane components of Rayleigh wave in rail steel

(b) Stress of 214.15 MPa

The lower plot in Fig. 6.25 shows the in-plane and out-of-plane signal for this case. Comparing it with the components at 5.36 MPa tells that the in-plane component drops down considerably. The mean value of polarization using velocity components is 0.13 and using displacement components is 0.24. The measurements show a standard deviation of 0.004. This is shown in Fig. 6.27 (a) and (b). The numerical simulation predicts a polarization of 0.659 which is about three times more than what is obtained experimentally. The theoretical values for Rayleigh wave speed, polarization and the expected change are shown in Table 6.2.

Table 6.2. Theoretically expected values

Stress [MPa]	c_R [m/s]	Π
5.36	2965.92	0.65841
214.15	2956.60	0.65965
Change	9.32	0.00123

Looking at the time domain signals shown in Fig. 6.26, it is observed that stressing the specimen reduces the phase difference between the signals drastically which ultimately almost cancels out the in-plane component. One explanation could be the presence of slight camber in the specimen cross-section, which causes additional movement of the two focusing points. Also, it can be observed that Rayleigh wave speed decreases as expected theoretically. However, the experimental change in Rayleigh wave speed is about nine times the expected change. The experimental values obtained are presented in Table 6.3.

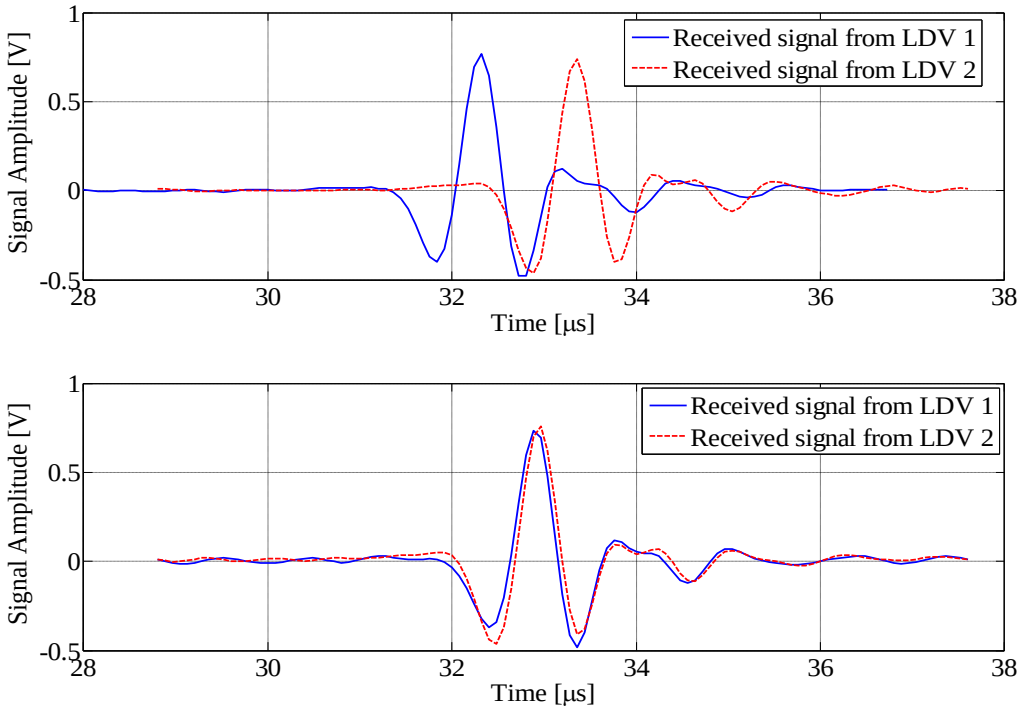

Fig. 6.26. Time domain representation of signals received by the two vibrometers. The upper plot is at 5.36 MPa and the lower plot is at 214.15 Mpa

Table 6.3. Experimental values

Stress [MPa]	Wave speed c_R [m/s]	Polarization Π
5.36	2964.48	0.4904
214.15	2880.58	0.1304
Change	83.9	- 0.36

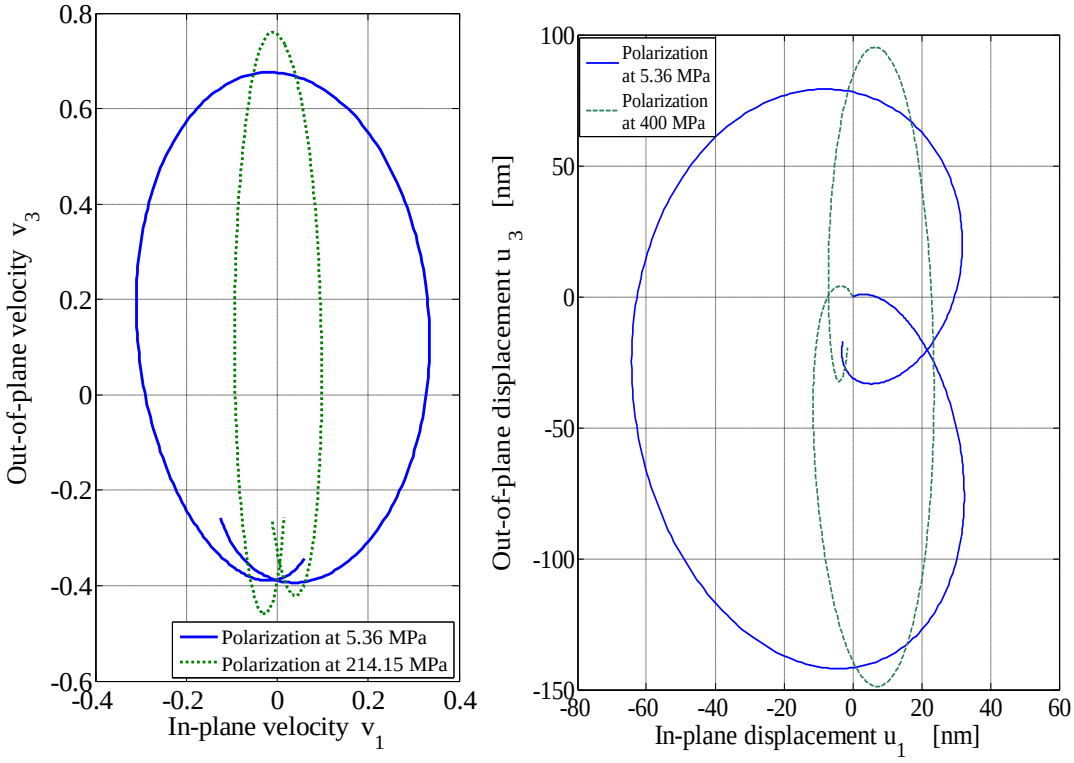

(a) Using velocity (b) Using displacement

Fig. 6.27. Rayleigh wave polarization at 5.36 MPa and 214.15 MPa.

The setup shown in Fig. 6.15 is also investigated, replacing the beam splitter and mirror by another LDV. The angle is taken as 22.5°. The results for this case are shown below. The upper plot in Fig. 6.28 shows the in-plane and out-of-plane components obtained at 5.36 MPa and the lower plot shows these components at 214.15MPa. It is clear that the two components have a phase shift other than $\pi/2$. The polarization is shown in Fig. 6.29. As expected the two ellipses do not show a vertical axis.

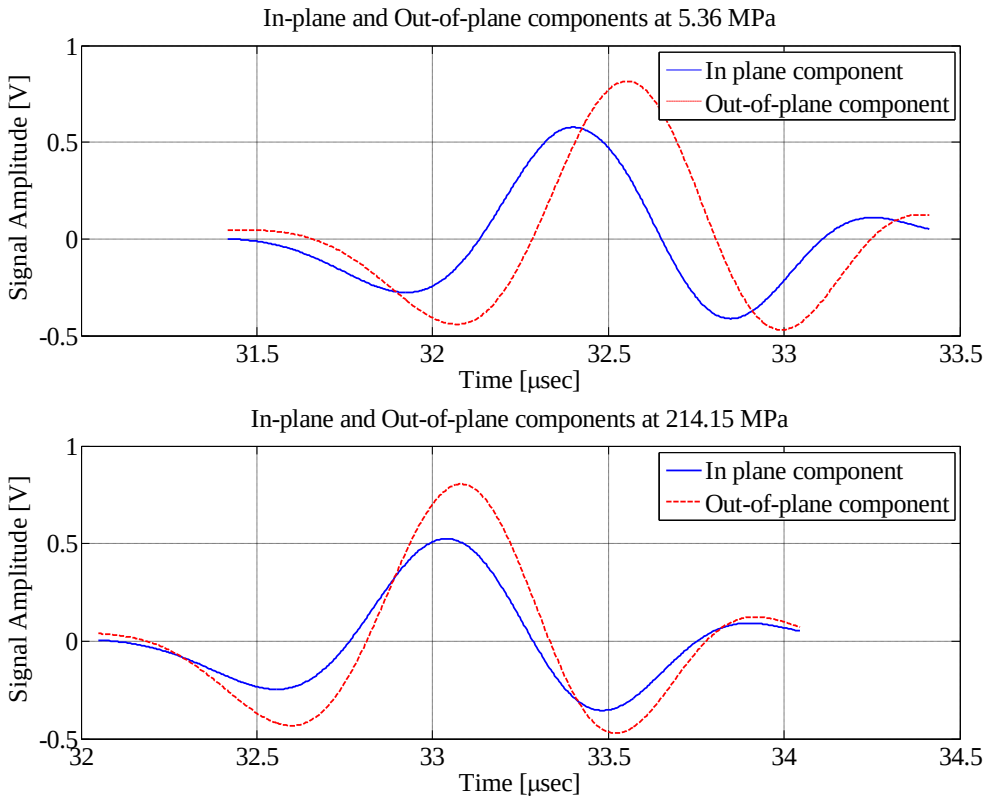

Fig. 6.28. In-plane and out-of-plane components of Rayleigh wave

In order to understand the effect of phase differences in the two signals, it is attempted to provide a phase shift to the received signals and plot the polarization thereafter. Fig. 6.30 shows the two signals after phase shifting such that the difference is $\pi/2$. The effect of phase shifting the signals is realized in the polarization presented in Fig. 6.31 and the corresponding polarization values are represented in Table 6.4 Although the change in polarization is larger than expected, the tendency of change in polarization agrees with the theory. In other words, polarization increases with increase in compression as shown by the simulations.

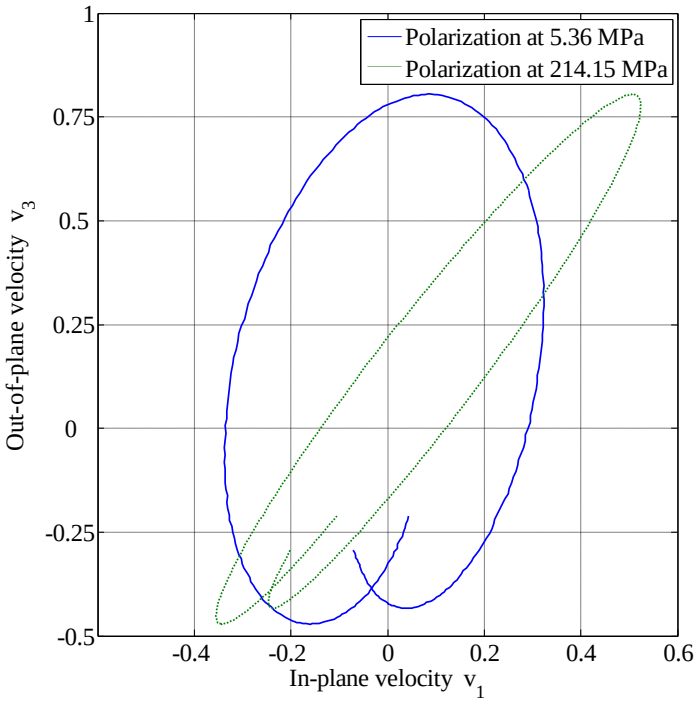

(a) Polarization using velocity components

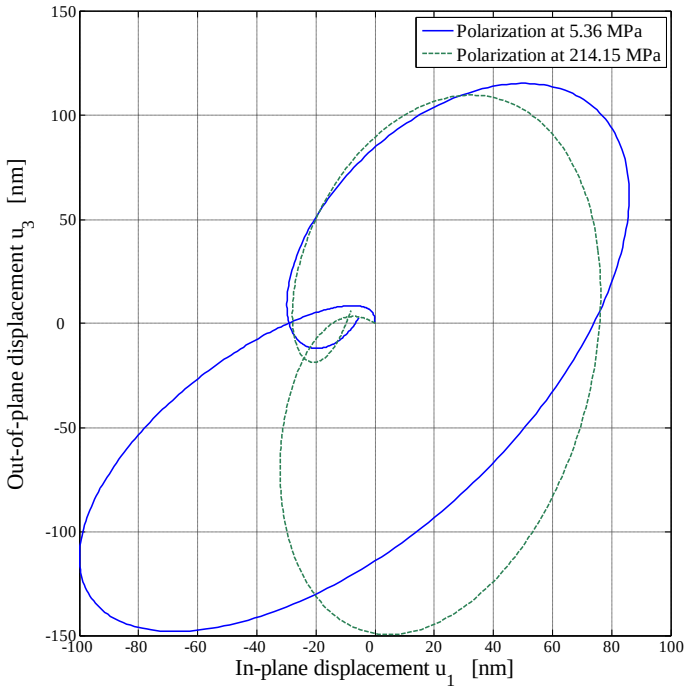

(b) Polarization using displacement components

Fig. 6.29. Rayleigh wave polarization at 5.36 MPa and 214.15 MPa

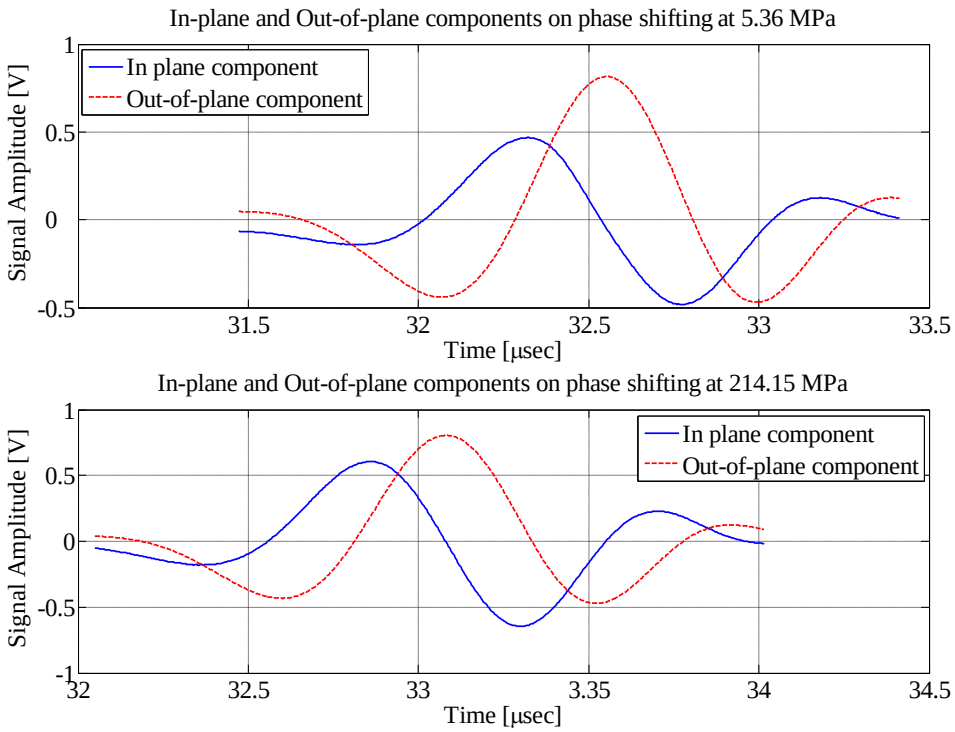

Fig. 6.30. In-plane and out-of-plane components of Rayleigh wave on phase shift

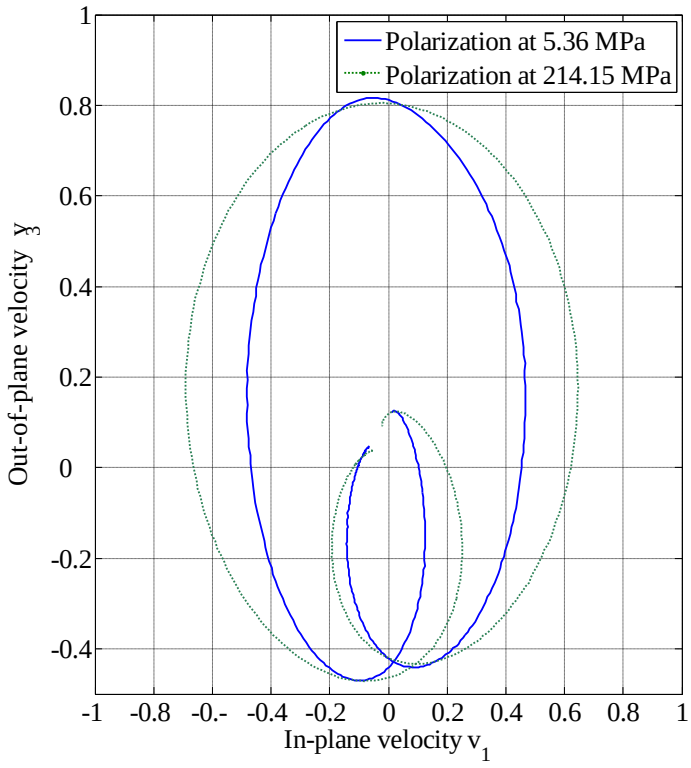

Fig. 6.31. Rayleigh wave polarization at 5.36 MPa and 214.15 MPa on phase shift

Table 6.4. Polarization values on phase shift

Stress [MPa]	Polarization Π
5.36	0.5736
214.15	0.8032
Change	0.23

6.5. Conclusion

Changes are observed in the Rayleigh wave speed and polarization on stressing the specimen. However, the changes are several times higher than expected. Rayleigh wave speed decreases with increase in stress which is consistent with the theory. However, polarization shows a decrease with increase in stress, contrary to the theory.

The most important reason for this discrepancy can be explained by the presence of camber in the specimen cross section which introduces the possibility of bending in the rail section. Several important conclusions that explain the discrepancy in the theory and experiments are explained in the next section.

CHAPTER VII

CONCLUSIONS AND FUTURE WORK

Using the acoustoelastic effect of ultrasonic waves, it is attempted to determine the applied stresses in rail steel. Initially, analytical models are developed for longitudinal, shear, Rayleigh and Lamb waves. Using numerical solution techniques, these models are evaluated to determine the sensitivity of acoustoelastic effect. A sensitivity analysis is carried out to determine the effect of variability in TOE constants on the acoustoelastic effect of Rayleigh waves. The solutions from numerical simulations reveal that the acoustoelastic effect of Rayleigh waves is more promising than that of other ultrasonic waves.

The proposed polarization measurement technique is known as the wedge-technique. In this, Rayleigh wave is generated using a transducer mounted on a plexiglass wedge. A laser Doppler vibrometer is used to detect the Rayleigh wave. In order to determine the polarization experimentally, several setups are investigated and the results compared. It is observed that using two laser Doppler vibrometers yielded better results. The rail specimen is subjected to a compressive stress in a testing machine and polarization measured for this case.

Finally, changes in Rayleigh wave speed and polarization are observed and compared to the expected changes predicted by the numerical simulation.

The following conclusions are made based on the results obtained from this research:

1. The results of the numerical simulation demonstrate that the acoustoelastic effect of Rayleigh wave speed is most sensitive among the ultrasonic waves investigated. The absolute change in wave speed is equal to 0.0447m/s/MPa and the sensitivity constant $k_c = 1.5\times10^{-5}$/MPa. Junge et al. (2004) states that the polarization of Rayleigh wave is

more sensitive than the wave speed. However, this is not true for all materials. From the analytical results obtained in this thesis it can be concluded that for rail steel Rayleigh wave speed is more sensitive than polarization.

2. The tendency of change in wave speed or polarization with stress depends on the TOE constants of the materials.

3. The effect of variability in TOE constants on the sensitivity of acoustoelastic effect is more prominent on Rayleigh wave polarization than on wave speed.

4. Different setups investigated reveal several important points to be considered for measuring polarization. Firstly, it is very important to record the in-plane and out-of-plane components at the exact same point. Secondly, a good reflective surface is necessary to obtain a better signal. Finally, it is important to maintain sufficient laser energy to avoid loss of carrier.

5. The experimentally observed changes in wave speed and polarization are several times higher than the values determined by the numerical simulations. A couple of reasons can be attributed to this discrepancy in the experimental and theoretical results.

- The excitation signal is not strong enough. This resulted into a very low SNR making the noise level higher than the decipherable changes in polarization.
- The experimental setup is subjected to a lot of floor vibrations. This might have added some noise to the signal.
- Temperature plays an important role in ultrasonic wave velocity. Changes in temperature during the experiment complicated the behavior of Rayleigh waves.
- The specimen is compressed in a machine that is suited for brute force crushing. As a result, the force applied is not constant and there is vertical vibration of the machine as it attempts to stabilize the force. Also, there is possibility of rigid body movement of the specimen before and after stressing such that the points of measurement are different.
- The reflective spray used to improve the reflectivity generates a speckle pattern on the rail surface. This speckle pattern adds some noise to the signal.

- The specimen cross section has a slight camber. As a result, part of the applied stress is initially used up in cancelling out the camber and the rest of the stress is effective. This causes additional movement of the signals detected by the vibrometers.

The following recommendations are suggested for future work:

1. **Excitation Signal**

It is observed that the vibrometer output is unsteady. A higher amplitude input signal might serve the purpose for obtaining a steady signal. Also, the LDV can be tuned to obtain a higher carrier signal.

2. **Reflectivity**

LDV works on the principle of comparing the incident or reference beam to the reflected beam. It is crucial that sufficient light is reflected, for further analysis. In this research, the rail specimen is coated with a reflective spray generating a speckle pattern. The received carrier signal is unstable, which may be attributed to the speckle pattern that adds some noise to the signal. A different method to improve the reflectivity of the surface needs to be investigated.

3. **Compressive Stress**

It is recommended to use a machine that can provide a constant stress without causing external vibrations.

4. **Measurement of Rayleigh Wave Components**

A method of measuring the in-plane and out-of-plane components by a single measurement would prove more effective. Junge (2004) used a type of LDV that could measure the in-plane and out-of-plane with a single measurement.

5. Camber

The cross section of the specimen needs to have exactly parallel faces. A slight camber would produce erroneous results as part of the stress is expended in nullifying the camber.

6. Texture

In order to completely understand the nature of the results and apply this stress measurement technique on a large scale, it will be necessary to evaluate the dependency of stress measurement on rail texture and variations in microstructure such as grain size or alloy content. For this purpose it is recommended to carry out a texture characterization for the rail sample and relate it to the stress measurement results.

REFERENCES

Allen D.R., Sayers C.M., (1984), "The Measurement of Residual Stress in Textured Steel Using an Ultrasonic Velocity Combinations Technique," *Ultrasonics*, 22(4), 179-188.

Bedford A., Drumheller D.S., (1996), *Introduction to Elastic Wave Propagation*, Wiley Publishers, 43-50, 106-111.

Bergman R.H., Shahbender R.A. (1958), "Effect of Statically Applied Stresses on the Velocity of Propagation of Ultrasonic Waves," *Journal of Applied Physics,*29.

Desmet C., Kawald U., Mourad A., Lauriks W., Thoen J. (1996), "The Behaviors of Lamb Waves in Stressed Polymer Foils," *Journal of Acoustical Society of America*, 100(3), 1509-1513.

Duquennoy M., Ouaftouh M., Qian M.L., Ourak M. (1999), "Ultrasonic Evaluation of Stresses in Orthotropic Materials Using Rayleigh Waves," *NDT&E International*, 32(4),189-199.

Egle D. M. and Bray D.E. (1976), "Measurement of Acoustoelastic and Third Order Elastic Constants for Rail Steel," *Journal of the Acoustical Society of America*, 60, 741-74.

Egle D. M. and Bray D.E. (1979), "Application of the Acousto-Elastic Effect to Rail Stress Measurements," *Materials Evaluation 37,* 41-55.

Espinola R.P., Waterman P.C. (1958), "An Ultrasonic Interferometer for Measurement of Velocity Changes in Solids," *Journal of Applied Physics*, 29, 718.

Graff K. (1978), *Wave Motion in Elastic Solids*, Dover Publications, New York.

Hughes D.S., Kelly J.L. (1953), "Second-Order Elastic Deformation of Solids," *Physical Review*, 92(5), 1145-1149.

Hurlebaus S., Jacobs L.J. (2006), "Dual Probe Laser Interferometer for Structural Health Monitoring," *Journal of the Acoustical Society of America*, 119(4), 1923-1925.

Hurlebaus S. (2005), "Smart Structures," *Lecture Notes*, Zachry Department of Civil Engineering, Texas A&M University, College Station, Texas.

Husson D., Bennett S. D., Kino G. S. (1982), "Measurement of Surface Stresses Using Rayleigh Waves," *Ultrasonics Symposium,* 889-892.

Jassby K., Kishoni D., (1983), "Experimental Technique for Measurement of Stress-Acoustic Coefficients of Rayleigh Waves," *Experimental Mechanics,* 23(1), 74-80.

Jones R. (1999), *Mechanics of Composite Materials,* Second Edition, Taylor & Francis, 60-67.

Junge M., Qu J., and Jacobs L.J., Jarzynski J., Saponara V. (2004), "The Measurement of Applied Stresses Using the Polarization of Rayleigh Waves," *Review of Quantitative Nondestructive Evaluation,* 23, 1187-1191.

Junge M. (2003), "Measurement of Applied Stresses Using the Polarization of Rayleigh Surface Waves," Masters Thesis, University of Stuttgart.

Kish A., Read D. (2006), "11th Annual AAR Research Review," *Transportation Technology Center Inc. (TTCI),* Pueblo CO.

Kish A., Samavedam G. (2005), "Improved Destressing of Continuous Welded Rail for Better Management of Rail Neutral Temperature," *Journal of the Transportation Research Board,* 1916, 56-65.

Lingfeng H. E., Kobayashi S., (2000), "Determination of stress-acoustic coefficients of Rayleigh Wave by Use of Laser Doppler Velocimetry," *JSME International Journal Series A-Solid Mechanics and Materials Engineering* 44(1), 17-22.

Lowe M. (1992), "Plate Waves for the NDT of Diffusion Bonded Titanium," PhD Thesis, Imperial College of Science, Technology and Medicine, University of London.

Murnaghan F.D. (1951), *Finite Deformation of an Elastic Solid,* Wiley, New York.

Pao Y., Gamer U. (1985), "Acoustoelastic Waves in Elastic Media," *Journal of Acoustical Society of America,* 77(3).

Pao Y., Sachse W., Fukuoka H. (1984), "Acoustoelasticity and Ultrasonic Measurements of Residual Stresses," *Physical Acoustics,* 17, 61:143.

Polytec, User Manual, Vibrometer Single point Sensor Head OFV-505/-503.

Railway Investigation Report, Transportation Safety Board of Canada, (2002 & 2003), Gatineau (Canada).

Rose J.L. (2004), *Ultrasonic Waves in Solid Media*, Cambridge University Press, 27-32.

Toupin R.A., Bernstein B. (1961), "Sound Waves in Deformed Perfectly Elastic Materials," *Journal of Acoustical Society of America,* 33(2), 216-225, 1961.

Tunna J. (2000), "Vertical Rail Stiffness Equipment (VERSE) TRIALS," *Letter Report* for Vortex International, Transportation Technology Center Inc. (TTCI), Pueblo CO.

Weaver R., Damljanović V. (2004), "Laser Vibrometry Technique for Measurement of Contained Stress in Railroad Rail," *Journal of Sound and Vibration,* 282 (2005), 341–366.

Wenk H. R., Houtte V. (2004), "Texture and Anisotropy," *Reports on Progress in Physics*, 67, 1367-1428.

VITA

Name:	Shailesh Gokhale
Address:	Texas A&M University, Zachry Department of Civil Engineering, College Station, TX-77843
Email :	shail008@gmail.com
Education:	B.E. Civil Engineering, Mumbai University, Mumbai, India, 2005 M.S. Civil Engineering, Texas A&M University, College Station, U.S.A., 2007